Applied Catalysis B: Environmental 340 (2024) 123234

Contents lists available at ScienceDirect

Applied Catalysis B: Environmental

journal homepage: www.elsevier.com/locate/apcatb

Elucidating the effect of Ce with abundant surface oxygen vacancies on $MgAl_2O_4$-supported Ru-based catalysts for ammonia decomposition

JungHun Shin [a], Unho Jung [a,*], Jiyu Kim [a,b], Kyoung Deok Kim [a,c], Dahye Song [a], Yongha Park [a], Byeong-Seon An [d], Kee Young Koo [a,e,**]

[a] Hydrogen Research Department, Korea Institute of Energy Research, 152 Gajeong-ro, Yuseong-gu, Daejeon 34129, Republic of Korea
[b] Department of Chemical & Biological Engineering, Korea University, 145 Anam-Dong, Seongbuk-Gu, Seoul 02841, Republic of Korea
[c] Graduate School of Energy Science and Technology, Chungnam National University (CNU), 99 Daehak-ro, Yuseong-gu, Daejeon 34134, Republic of Korea
[d] Analysis Center for Energy Research, Korea Institute of Energy Research (KIER), 152 Gajeong-ro, Yuseong-gu, Daejeon 34129, Republic of Korea
[e] Advanced Energy and System Engineering, University of Science and Technology (UST), 217 Gajeong-ro, Yuseong-gu, Daejeon 34113, Republic of Korea

ARTICLE INFO

Keywords:
Ammonia decomposition
Hydrogen production
Oxygen vacancy
Ceria promoter
Ruthenium structure

ABSTRACT

Ammonia is a promising CO_x-free hydrogen (H_2) carrier because of its high volumetric H_2 density. However, developing highly active/stable ammonia decomposition catalysts for H_2 production remains challenging. In this study, the role of ceria (CeO_2) as a promoter for Ru-based catalysts was investigated. $Ru/Ce_x/MgAl_{(y00)}$ catalysts were prepared by the incipient wetness impregnation (IWP) and deposition–precipitation (DP) methods. The surface oxygen vacancy (OV) concentration was controlled by the Ce loading and calcination temperature. By evaluating the surface reaction behavior of the ammonia decomposition catalysts, this study proposes that CeO_2 effectively improves the recombination/desorption of N and H atoms. The optimal catalyst $Ru/Ce_5/MgAl_{(600)}$ achieved a high H_2 formation rate (27.4 $mmol H_2 \cdot g_{cat}^{-1} \bullet min^{-1}$ at 30,000 $mL \cdot g_{cat}^{-1} \cdot h^{-1}$, 450 °C) and stable performance after exposure at 650 °C for 20 h. This study provides insight into the effect of abundant surface OVs in CeO_2 on the physicochemical properties and ammonia decomposition performance of the catalysts.

1. Introduction

Hydrogen (H_2) has been proposed as an alternative to fossil fuels because of its ability to store energy for long periods and its environmental friendliness owing to its carbon-free nature, which can complement the variability of renewable energy sources [1–3]. Various countries are pursuing large-scale clean H_2 production projects based on renewable energy to prepare for the transition to environmentally friendly energy. Ammonia is attracting considerable attention as a H_2 carrier owing to its high H_2 storage capacity, with a volumetric H_2 density of 121 kg-H_2/m^3, which is higher than that of liquid H_2 [4,5]. Ammonia is an environmentally friendly H_2 carrier because it does not emit CO_2, and it is economical because it can be easily liquefied under mild storage conditions (27 °C, 8 atm) [4,5]. Additionally, the infrastructure for ammonia synthesis (the Haber–Bosch process) and marine transportation has already been established internationally, making ammonia an attractive H_2 carrier [6]. However, to obtain H_2 from ammonia, the energy supply required to operate high-temperature ammonia decomposition reactors should be considered [4]. Furthermore, limiting unreacted ammonia to the extent possible is crucial during ammonia decomposition to obtain high-purity H_2 [4].

Ammonia decomposition occurs via the stepwise dissociation of ammonia adsorbed on Lewis acid sites, followed by the recombination of N and H atoms to produce N_2 and H_2 [7]. Ganley et al. [8] estimated the scission rate of N-H bonds and the recombination rate of N atoms for various active metals using the Blowers–Masel equation, and they proposed a rate-determining step (RDS) based on a correlation between ammonia decomposition performance and theory. Furthermore, their correlation-derived volcano curve revealed that the balance between the two RDSs is crucial and that the primary RDS varies depending on the active metal properties [8]. Ru exhibits superior performance in ammonia decomposition and has optimal conditions for both the RDSs [8–11]. However, owing to the scarcity and high cost of Ru, the development of inexpensive catalysts has been receiving increasing interest. To address this issue, a facile and efficient method for manufacturing Ru-based catalysts is required.

* Corresponding author.
** Corresponding author at: Hydrogen Research Department, Korea Institute of Energy Research, 152 Gajeong-ro, Yuseong-gu, Daejeon 34129, Republic of Korea.
E-mail addresses: uhjung@kier.re.kr (U. Jung), kykoo@kier.re.kr (K.Y. Koo).

https://doi.org/10.1016/j.apcatb.2023.123234
Received 17 May 2023; Received in revised form 3 August 2023; Accepted 27 August 2023
Available online 28 August 2023

Carbon-based materials have attracted considerable attention as supports for Ru-based ammonia decomposition catalysts [11,12]. However, carbon-based supports suffer from severe carbon depletion owing to methanation reactions that occur in an H_2 atmosphere, which leads to decreased stability [12]. Therefore, various oxide supports, such as Ru/Al_2O_3 [13], Ru/La_2O_3 [14], and Ru/MgO [15,16], have been proposed for ammonia decomposition. These supports have the advantage of controlling the structure and electronic properties of the active metal via metal-support interactions (MSI). Recently, the most effective catalyst design approach for ammonia decomposition has involved the use of promoters with excellent electron-donating abilities on the support to improve the physicochemical properties of the catalyst. Alkali (Cs, K, and Na) and alkaline earth (Mg, Ca, and Ba) metals have been used as promoters to donate electrons to the active metal during ammonia decomposition [17–19]. The recombination of adsorbed N atoms was reported to be the RDS in ammonia decomposition and the nitrogen adsorption strength of Ru was reduced by the electrons received from electron donors, which facilitated desorption.

Ceria (CeO_2) is attracting attention as an electron donor in catalytic reactions because of its high oxygen storage capacity (OSC), which supplies electrons via abundant defects under reducing conditions [20,21]. Additionally, it has a high electron transfer capacity owing to its excellent redox cycle properties based on the reversibility of Ce^{3+}/Ce^{4+} [22,23]. Recently, CeO_2 has been evaluated in Ru-based catalysts for ammonia decomposition. Hu et al. [24] reported that Ru clusters anchored on CeO_2 exhibit superior ammonia decomposition performance and stability owing to strong MSIs. Additionally, Le et al. [25]. reported improved N_2/H_2 desorption owing to the strong interactions between the highly basic sites of $La_xCe_{1-x}O_y$ composites and the exposed Ru sites. However, the role of CeO_2 in Ru-based ammonia decomposition catalysts remains unclear, and CeO_2 has not yet been reported as a promoter in these systems.

Therefore, this study proposes a potential method for utilizing CeO_2 as a promoter to design Ru-based catalysts with high efficiency and stability for ammonia decomposition at low temperature. Moreover, this study aims to propose the role of CeO_2 as a promoter. Compared to CeO_2-supported catalysts, the use of CeO_2 as a promoter with an appropriate support can provide a larger surface area and improved thermal stability, which is advantageous for Ru-Ce interactions. CeO_2 is added to $MgAl_2O_4$-spinel supports, which have high specific surface areas and thermal stabilities, using the incipient wetness impregnation (IWI) method. Subsequently, Ru is added to the $Ce/MgAl_2O_4$ surface using the deposition–precipitation (DP) method. The developed synthesis method is suitable for commercialization because it can be applied to preformed $MgAl_2O_4$ supports in the pellet or bead form. Controlling the Ce content and calcination temperature influenced the formation of oxygen vacancies (OVs). Therefore, the influence of OVs on the interaction of Ru with CeO_2 and the physicochemical properties of the catalysts is investigated. Finally, the effects of catalytic properties on ammonia decomposition reactions are discussed.

2. Experimental

2.1. Catalyst preparation

2.1.1. Ce/MgAl preparation

Ce/MgAl was prepared using the incipient wetness impregnation (IWI) method. The support material $MgAl_2O_4$-LDH (PURALOX MG30, Sasol Co.) was calcined at 800 °C for 8 h in an air atmosphere to produce a thermally stable spinel structure. The CeO_2 content was calculated to be 2.5–10 wt% of the $MgAl_2O_4$-spinel support, and aqueous solutions were prepared by dissolving the required amount of cerium nitrate ($Ce(NO_3)_3 \bullet 6\,H_2O$, Aldrich Chemical Co.) in a solution volume 1.2 times the total pore volume of the support. The impregnated powder was dried for 6 h at 25 °C and then at 100 °C overnight in an oven. Finally, the powder was heated up to 500–800 °C at a rate of 4 °C/min in an air atmosphere and calcined for 6 h. The calcined samples were denoted as $Ce_x/MgAl_{(y00)}$, where x and y represent the CeO_2 content and calcination temperature, respectively.

2.1.2. Preparation of Ru/MgAl and Ru/Ce/MgAl

Ru-based catalysts were prepared using the deposition–precipitation (DP) method, which is commonly used to synthesize precious metals and metal oxide supports [26]. The Ru content was calculated to be 2 wt% of MgAl or $Ce_x/MgAl_{(y00)}$, and a 1.5 % w/v ruthenium nitrosylnitrate solution ($Ru(NO)(NO_3)_x(OH)_y$, Alfa Aesar Co.) was prepared. The Ru solution was mixed with 500 mL of distilled water containing MgAl or $Cex/MgAl_{(y00)}$. Subsequently, a urea solution with a urea-to-Ru molar ratio of 200:1 was prepared as the precipitating agent and mixed with the Ru solution by stirring. The mixture was reacted for 8 h at 80 °C and then aged for 12 h at room temperature. The precipitate was filtered, washed with deionized water at least three times, and then dried overnight at 100 °C. Finally, the obtained powder was reduced at 600 °C for 3 h in a 10% H_2/Ar atmosphere. The catalysts were denoted as Ru/MgAl or $Ru/Ce_x/MgAl_{(y00)}$.

2.2. Catalytic activity

The NH_3 decomposition activity of the $Ru/Ce_x/MgAl_{(y00)}$ catalysts was evaluated in a fixed-bed reactor. The prepared catalyst (140–104 μm, 100 mg) was mixed with an inert diluent ($MgAl_2O_4$) at a 1:5 mass ratio to eliminate temperature and concentration gradients, and packed into a quartz tube with an inner diameter of 6 mm. The sample was pretreated at 600 °C in an H_2 atmosphere for 1 h, and the pure NH_3 gas used in the ammonia decomposition experiment was injected at a constant rate using a mass flow controller. Subsequently, ammonia decomposition was evaluated at a reaction temperature of 350–600 °C (temperature decreased at a rate of 1 °C/min) and weight hourly space velocity (WHSV) of 30,000 $mL \cdot g_{cat}^{-1} \bullet h^{-1}$. The products were monitored using an online gas chromatograph (GC; 7890 GC; Agilent Co.) equipped with a thermal conductivity detector (TCD). A PoraPLOT amine capillary column (Agilent Co.) and He carrier gas were used for NH_3 analysis, and an HP-PLOT 5 A column (Agilent Co.) and Ar carrier gas were used for H_2 and N_2 analyses.

The NH_3 conversion ($X_{NH3,}$ %) was calculated using Eq. (1). Here, F_{NH3in} represents the flow rate of NH_3 entering the reactor and F_{NH3out} represents the flow rate of NH_3 measured at the outlet of the catalyst bed.

$$NH_3 \quad \text{conversion}(XNH3, \%) = \frac{F_{NH3in} - F_{NH3out}}{F_{NH3in}} \times 100 \tag{1}$$

The HSC chemistry® 7.1 software was used to calculate the thermodynamic equilibrium value of NH_3, N_2, and H_2 in the reaction. Kinetic studies were conducted without diffusion limitations using an NH_3 conversion below 20 % and WHSVs of 30,000–480,000 $mL \cdot g_{cat}^{-1} \bullet h^{-1}$. A diluent was used to maintain a constant catalyst bed volume. The activation energy (E_a) of each catalyst was calculated using the Arrhenius equation (Eq. (2)), where k is the reaction rate constant, A is the frequency factor, R is the gas constant, and T is the absolute temperature.

$$k = A\exp\left(\frac{-E_a}{RT}\right) \tag{2}$$

The H_2 formation rate was calculated using Eq. (3), where m_{cat} is the catalyst mass. The turnover frequency (TOF) was calculated using Eq. (4) based on the calculated H_2 formation rate (r_{H2}) and the number of active sites, where A_{Ru} is the molar mass of Ru, D_{Ru} is the dispersion of Ru, and W_{Ru} is the weight fraction of Ru in the catalyst.

$$H_2 \quad \text{formation rate}(r_{H2}, \text{mmol}_{H2} \Big/ \text{min} \bullet \text{gcat}) = \frac{\frac{F_{NH3in}}{22.4} \bullet X_{NH3} \bullet 1.5}{m_{cat}} \tag{3}$$

$$\text{Turnover frequency}(\text{TOF}, s^{-1}) = \frac{r_{H2} \bullet A_{Ru}}{D_{Ru} \bullet W_{Ru}} \quad (4)$$

The stabilities of Ru/MgAl and Ru/Ce_5/$MgAl_{(600)}$ were evaluated in the temperature range of 450–650 °C at a WHSV 30,000 and 240,000 mL·g_{cat}^{-1}•h^{-1}, respectively. Each sample was pretreated at 600 °C in a reducing atmosphere (10 % H_2/He) for 1 h and then cooled to 450 °C in a He atmosphere. Subsequently, pure NH_3 was injected, and the NH_3 concentration was measured at fixed temperatures of 450 and 500 °C for approximately 20 h at 40 min intervals. The stabilities of the samples were evaluated prior to thermal aging at high temperatures. Thermal aging at elevated temperatures shortens the observation time for determining catalyst durability. Subsequently, the catalysts were exposed to pure NH_3 at 650 °C for 20 h, and the performance was measured at fixed temperatures of 450 and 500 °C for approximately 20 h. The catalyst performance before and after thermal aging was compared based on the $X_{NH3}/X_{NH3,initial}$ ratio, which is an indicator of the stability of the initial catalyst performance. Here, $X_{NH3,initial}$ represents the initial NH_3 conversion of the catalyst at each temperature, and X_{NH3} represents the NH_3 conversion over the reaction time.

2.3. Catalyst characterization

The specific surface areas and pore size distributions of the catalyst samples were measured using a BELSORP-MAX instrument (MicrotracBEL Co.) and calculated using the Brunauer–Emmett–Teller (BET) and Barrett–Joyner–Halenda (BJH) methods, respectively. The samples were pretreated under vacuum at 300 °C for 3 h, and then their N_2 adsorption/desorption isotherms were measured at − 196 °C.

The elemental compositions of the catalyst samples were analyzed by inductively coupled plasma–mass spectrometry (ICP–MS) on an Agilent ICP-MS 7700 S instrument (Agilent Co.). Prior to ICP–MS analysis, the samples were pretreated using a solution of 70 % HNO_3 and 30 % HCl in a microwave reactor to achieve complete dissolution.

The crystal structures of the catalysts were characterized by X-ray diffractometer (XRD) on a SmartLab High Temp instrument (Rigaku Co.), with Cu Ka radiation (λ = 0.154 nm). XRD spectra were measured in the 2θ range of 20–80° at a rate of 2°/min.

The dispersion of the active metals on the catalysts was estimated by CO pulse chemisorption using a BEL-METAL-3 instrument (MicrotracBEL Co.). The sample was reduced with 10 % H_2/Ar gas at 600 °C for 1 h and then cooled to 50 °C in an Ar atmosphere.

For transmission electron microscopy (TEM) analysis, samples were prepared using the conventional drop-casting method. An analytical transmission electron microscope (JEM-ARM 200 F NEOARM, JEOL, Germany) coupled with a dual-type energy-dispersive X-ray spectrometer (JED-2300 T, JEOL Ltd.) was used to detect single Ru atoms and crystalline and amorphous CeO_2 phases in the MgAl matrix. The elemental distributions of Ru, Ce, and O were determined by scanning transmission electron microscopy–energy-dispersive X-ray spectroscopy (STEM–EDS) mapping.

The valence states of the catalyst surfaces were characterized by X-Ray photoelectron spectroscopy (XPS) using a Sigma Probe instrument (Thermo VG Scientific Co.). Samples were prepared under a vacuum of 10^{-9} Torr and measured using an X-ray source with Al Kα radiation (1486.7 eV). The sample spectra were calibrated to the peak corresponding to the C 1 s band at 284.6 eV, and the bands corresponding to Ru 3d, Ce 3d, and O 1 s were deconvoluted using Gaussian/Lorentzian functions.

The surface structural characteristics of the catalyst samples were characterized by high-resolution Raman spectroscopy using a LabRam HR Evolution Visible–NIR instrument (HORIBA Co.) and an output power of 0.3 mW. The samples were focused using a 514 nm Ar-ion laser, and the Raman shift was measured in the range of 500–2000 cm^{-1}.

The redox properties and interaction between the active metal and the support were characterized by H_2-temperature programmed reduction (H_2-TPR) using a BELCAT-B instrument (MicrotracBEL Co.). Each sample (50 mg) was loaded into the reactor and pretreated in an Ar atmosphere at 400 °C for 30 min to remove surface impurities and moisture. After cooling the sample to 60 °C, it was treated in a 5 % O_2/He and 10 % H_2/Ar atmosphere for 1 h and stabilized. Subsequently, the sample was heated to 1020 °C at a rate of 10 °C/min in a 10 % H_2/Ar atmosphere, and H_2 consumption was measured using a TCD.

The desorption properties of the catalysts were characterized by NH_3-temperature programmed desorption (NH_3-TPD) and CO_2-temperature programmed desorption (CO_2-TPD) using the BELCAT-B instrument. Each sample (100 mg) was pretreated in a 10 % H_2/Ar atmosphere at a heating rate of 10 °C/min up to 600 °C for 1 h. After removing the adsorbed H species on the catalyst surface under He gas flow for 1 h, the sample was cooled to 50 °C. Subsequently, the sample was exposed to a 10 % NH_3/He or 10 % CO_2/He atmosphere at 50 °C for 1 h, and then weakly physisorbed species were desorbed under He gas flow for 1 h. Subsequently, the sample was heated to 800 °C at a rate of 10 °C/min. Desorbed NH_3 or CO_2 was measured using a TCD coupled with a quadrupole mass spectrometer (MicrotracBEL Co.).

The electron transfer and surface reaction behaviors of the catalysts were characterized by in situ diffuse reflectance infrared Fourier transform spectroscopy (in situ DRIFTS) using a Nicolet iS50 FTIR spectrometer (Thermo Fisher Scientific). Data were collected from 64 scans at a resolution of 4 cm^{-1}. The diffuse reflectance (DR) spectrometer was equipped with a deuterated triglycine sulfate (DTGS) detector and a ZnSe window attached to the reaction chamber. The samples were pretreated at 400 °C for 1 h in a 10 % H_2/He atmosphere to remove impurities and moisture. Subsequently, the sample was exposed to a 10 % CO/He or 10 % NH_3/He atmosphere at 50 °C for 1 h, and desorption was conducted in a He atmosphere in the temperature range of 50–300 °C.

3. Results and discussion

3.1. Ammonia decomposition activity

In this study, the influence of CeO_2 on the ammonia decomposition performance of Ru-based catalysts supported on $MgAl_2O_4$ was investigated. The properties of CeO_2 are closely related to the catalytic performance, and therefore they should be carefully controlled. Thus, the CeO_2 content and calcination temperature were controlled because they significantly affect the catalyst performance. The catalysts were prepared using 2.0 (± 0.15) wt% of Ru loaded onto the support. As shown in Fig. 1(a) and (b), the NH_3 conversion was determined at a WHSV of 30,000 mL·g_{cat}^{-1}•h^{-1} in the temperature range of 600–350 °C. The NH_3 conversion of the catalyst improved with increasing reaction temperature, which is consistent with the endothermic nature of the ammonia decomposition reaction. The Ru/MgAl catalyst achieved an NH_3 conversion of 50 % at approximately 465 °C, and exhibited a performance of 99.5 % at temperatures above 550 °C. In contrast, Ce-promoted catalysts exhibited a significant increase in performance at low temperatures (below 550 °C). In particular, Ru/Ce_5/$MgAl_{(600)}$ exhibited the highest performance, achieving an NH_3 conversion of 99.5 % at temperatures above 500 °C. Fig. 1(b) shows the catalytic performance of Ru/Ce_5/$MgAl_{(y00)}$ as a function of the CeO_2 calcination temperature. The optimal calcination temperature of CeO_2 for ammonia decomposition was 500–600 °C, whereas NH_3 conversion decreased at temperatures above 700 °C. Therefore, the addition of Ce as a promoter improved the ammonia decomposition performance. Moreover, the CeO_2 content and calcination temperature affected the catalyst performance.

Fig. S1 shows the NH_3 conversion of the Ru/MgAl and Ru/Ce_5/$MgAl_{(600)}$ catalysts as a function of the WHSV. At a reaction temperature of 450 °C, Ru/MgAl exhibited a performance of approximately 20 % at a WHSV of 60,000 mL·g_{cat}^{-1}•h^{-1}. Ru/Ce_5/$MgAl_{(600)}$ exhibited an

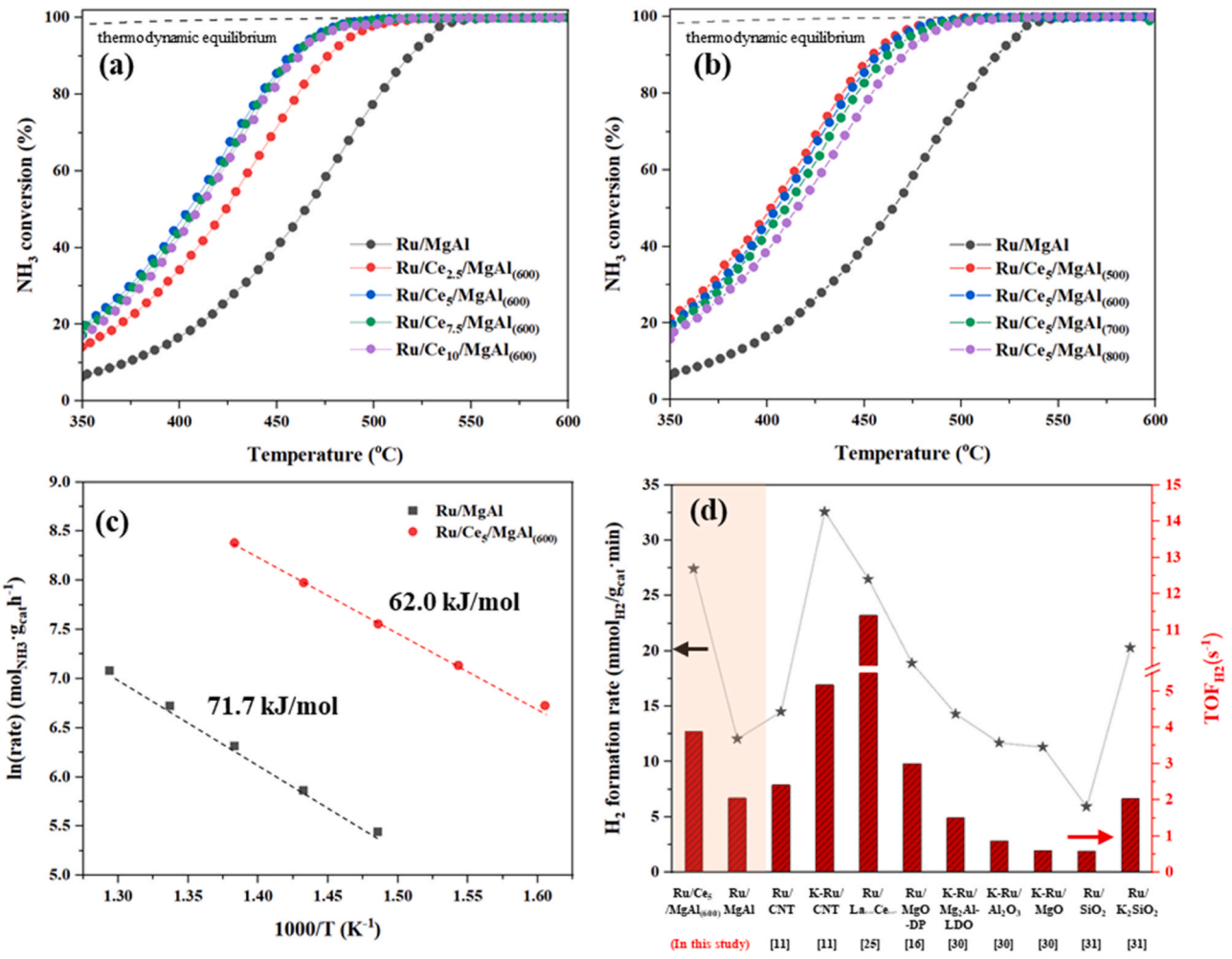

Fig. 1. Ammonia decomposition performance of $Ru/Ce_x/MgAl_{(y00)}$ catalysts as a function of (a) Ce loading and (b) Ce calcination temperature (Inlet gas: pure NH_3, WHSV: 30,000 mL/g_{cat}•h). Dash line corresponds to the equilibrium conversion on ammonia decomposition. (c) Arrhenius plots to determine the activation energy for ammonia decomposition over the Ru/MgAl and $Ru/Ce_5/MgAl_{(600)}$ catalysts. (d) Comparison of the H_2 formation rate and TOF_{H2} of the Ru/MgAl and $Ru/Ce_5/MgAl_{(600)}$ catalysts at 450 °C and WHSV = 30,000 mL/g_{cat}•h with previously reported ammonia decomposition catalysts.

equivalent performance at a WHSV of 480,000 $mL \cdot g_{cat}^{-1} \cdot h^{-1}$, which is approximately eight times higher than that of Ru/MgAl. Fig. 1(c) shows the Arrhenius plot of the reaction rate as a function of temperature, which had a negative slope that was used to calculate the activation energy. The activation energies of Ru/MgAl and $Ru/Ce_5/MgAl_{(600)}$ were 71.7 and 62.0 kJ/mol, respectively. Therefore, the $Ru/Ce_5/MgAl_{(600)}$ catalyst has a lower activation energy than those reported for Ru-based catalysts supported on oxide metals (67.3–121.7 kJ/mol)[15,27–29]. The lower reaction barrier of $Ru/Ce_5/MgAl_{(600)}$ owing to Ce addition is comparable to that of the alkali-modified 4.8 % K-Ru/CNT catalyst with a high Ru loading (55.7 kJ/mol) [11]. To evaluate the ammonia decomposition rate, the r_{H2} and TOF were calculated based on the surface metal atoms of the catalyst. The Ru content and dispersion used to calculate the TOF of the catalysts were determined by ICP–MS and CO-pulsed chemisorption, respectively (Table S1). The r_{H2} and TOF of various ammonia decomposition catalysts were compared with those reported in previous studies, as presented in Fig. 1(d) and Table S2. The r_{H2} of $Ru/Ce_5/MgAl_{(600)}$ was 27.44 $mmol_{H2} \cdot g_{cat}^{-1}$•$min^{-1}$, which is faster than the conventional ammonia decomposition catalysts except for K-Ru/CNTs (29.9 $mmolH_2 \cdot g_{cat}^{-1}$•$min^{-1}$). Although the K-Ru/CNTs catalyst is reported to exhibit excellent performance in ammonia decomposition, the high Ru content (4.8 wt%) and potential instability of the support due to methanation reactions in an H_2 atmosphere are concerning. It is noteworthy that $Ru/Ce_5/MgAl_{(600)}$ exhibited a superior H_2 formation rate, even at low Ru contents, compared with those of previously reported oxide supported Ru-based catalysts [14,16,24,25,30,31]. In terms of TOF, the $Ru/La_{0.33}Ce_{0.67}$ catalyst exhibited higher value compared to the other catalysts in Fig. 1(d). However, the r_{H2} of $Ru/La_{0.33}Ce_{0.67}$ catalyst is slightly lower than that of $Ru/Ce_5/MgAl_{(600)}$ catalyst. It is because that the metal dispersion of the $Ru/Ce_5/MgAl_{(600)}$ catalyst is nearly three times higher (60.11 %) than that of the $Ru/La_{0.33}Ce_{0.67}$ catalyst (21.7 %) [25]. The TOF of $Ru/Ce_5/MgAl_{(600)}$ (450 °C, WHSV = 30,000 $mL \cdot g_{cat}^{-1}$•h^{-1}) was improved (3.89 s^{-1}) compared with that of MgAl (2.05 s^{-1}), indicating that the active sites of the $Ru/Ce_5/MgAl_{(600)}$ catalyst promote H_2 production. The r_{H2} and TOF of the $Ru/Ce_5/MgAl_{(600)}$ catalyst was further evaluated under kinetic conditions (<20 % NH_3 conversion) without mass transfer limitations (450 °C and 480,000 $mL \cdot g_{cat}^{-1} \cdot h^{-1}$). As listed in Table S2, the r_{H2} and TOF were significantly high, reaching 109.0 $mmol_{H2} \cdot g_{cat}^{-1} \cdot min^{-1}$ and 15.42 s^{-1}, respectively.

The stability of Ru/MgAl and $Ru/Ce_5/MgAl_{(600)}$ for ammonia decomposition was evaluated before and after thermal aging at 650 °C for 20 h. The NH_3 conversion of the catalysts was measured at 450 and 500 °C for 20 h, under conditions of < 80 % NH_3 conversion. Ru/MgAl and $Ru/Ce_5/MgAl_{(600)}$ exhibited similar performances at different WHSVs, are shown in Fig. 2(a) and (b). The NH_3 conversion before and after thermal aging of $Ru/Ce_5/MgAl_{(600)}$ was higher than that of Ru/MgAl, although the WHSV used for Ru/MgAl was eight times higher

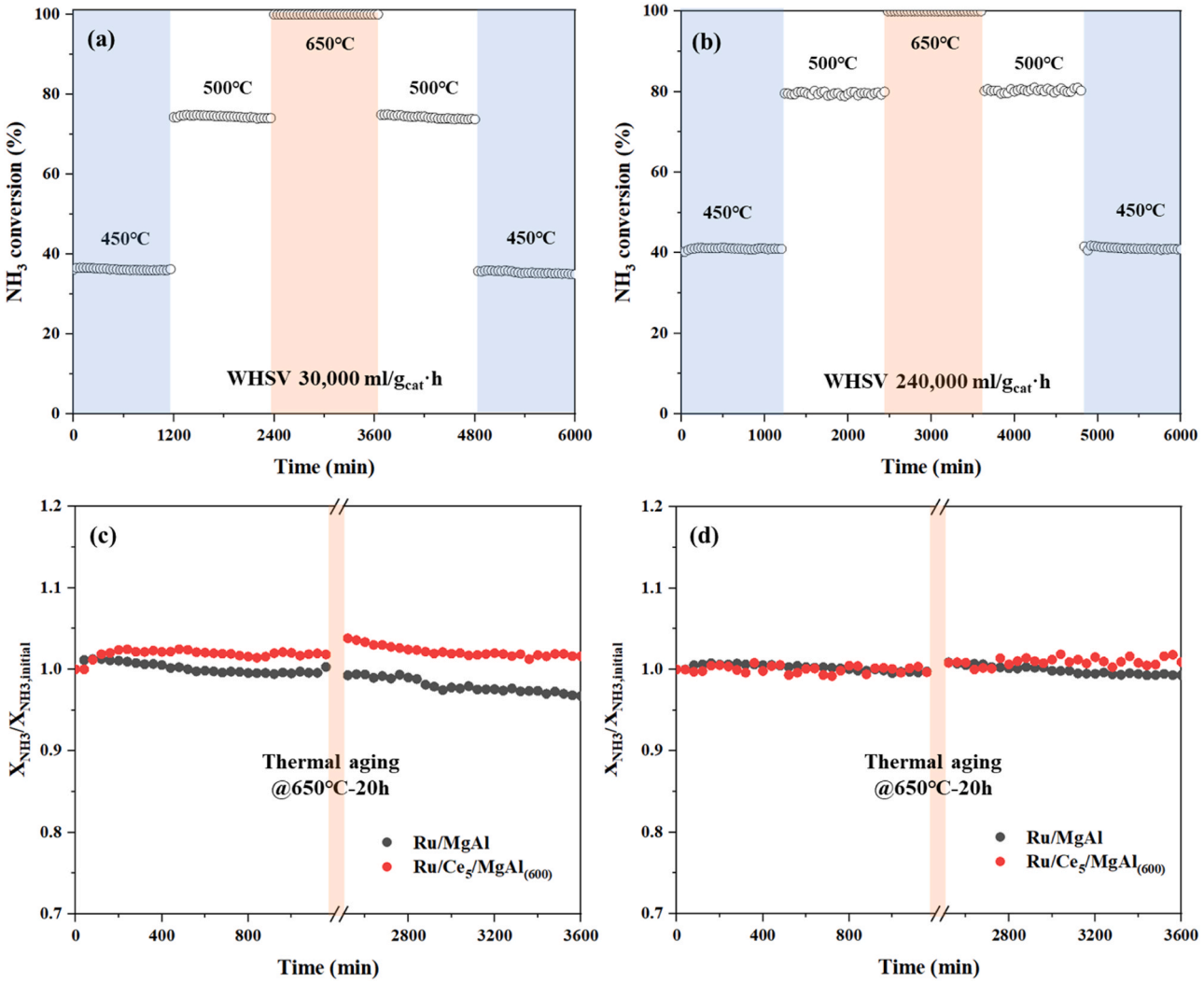

Fig. 2. Long-term stability test at various temperatures of the (a) Ru/MgAl and (b) Ru/Ce_5/$MgAl_{(600)}$ catalysts. The effect of thermal aging on relative activity (X_{NH3}/$X_{NH3,initial}$) at (c) 450 °C and (d) 500 °C.

than that used for Ru/Ce_5/$MgAl_{(600)}$. The X_{NH3}/$X_{NH3,initial}$ ratios were calculated to compare the ammonia decomposition stability over time based on the experimental results obtained in Fig. 2(a) and (b). As shown in Fig. 2(c), the X_{NH3}/$X_{NH3,initial}$ ratio increased during the initial reaction (approximately 40–80 min) before thermal aging owing to surface stabilization at 450 °C. The ammonia decomposition performance (in terms of the X_{NH3}/$X_{NH3,initial}$ ratio) of Ru/Ce_5/$MgAl_{(600)}$ remained constant after thermal aging, whereas that of Ru/MgAl decreased by 0.045. Fig. 2(d) shows the X_{NH3}/$X_{NH3,initial}$ ratio at 500 °C, and both samples exhibited an insignificant change in performance. This indicates that deactivation induced by thermal aging is more pronounced at lower temperatures. The deactivation of metal-oxide-supported Ru-based catalysts during ammonia decomposition is mainly attributed to sintering, diffusion, and volatilization induced by thermal aging [32]. These results demonstrate that CeO_2 contributes to the stable performance of the Ru/Ce_5/$MgAl_{(600)}$ catalyst, even after thermal aging, and improves the H_2 formation rate per unit time.

3.2. *Characteristics of the Ru/Ce_x/$MgAl_{(y00)}$ catalysts*

The XRD patterns in Fig. S2 show that Ce addition led to an increase in the peaks corresponding to ceria with a cubic fluorite structure (JCPDF No. 00–002–1306) on the surface of spinel-structured $MgAl_2O_4$ (JCPDF No. 00–001–1154). A diffraction peak corresponding to metallic Ru (JCPDF No. 00–006–0663) was not detected, indicating that the Ru present in the catalyst has a very small size [33]. As listed in Table S1, the BET specific surface areas (S_{BET}) of the catalysts decreased with increasing Ce content or calcination temperature. This phenomenon may be attributed to the agglomeration of excess or sintered CeO_2, causing blockage of the $MgAl_2O_4$ pores [34,35].

The Cs-corrected STEM images combined with EDS mapping show the morphology and distribution of Ru and CeO_2 dispersed on the MgAl spinel surface. Based on the low-magnification STEM–EDS images of Ru/MgAl shown in Fig. 3(a), Ru nanoclusters (NCs) with a size of approximately 1–2 nm were evenly distributed on the MgAl surface, which is consistent with the XRD pattern. The high-magnification STEM images shown in Fig. S3 clearly reveals the structure of the Ru NCs, which had a hexagonal shape with rounded corners and a lattice spacing of 0.21 nm, corresponding to the (101) plane. The low-magnification STEM image of Ru/Ce_5/$MgAl_{(600)}$ shown in Fig. 3(b) indicates the distribution of CeO_2 nanoparticles or amorphous particles with sizes in the range of 3–7 nm, on the MgAl support surface. Furthermore, the particle size distribution analysis of Ru revealed that the average particle size of Ru/Ce_5/$MgAl_{(600)}$ was approximately 0.6 nm smaller than that of Ru/MgAl, indicating a higher dispersion. Based on the high-resolution STEM (HR-STEM) image of Ru/Ce_5/$MgAl_{(600)}$ shown in Fig. 4, hemispherical nanoceria were observed, with a lattice spacing of 0.31 nm corresponding to the (111) crystal plane. Additionally, the lattice spacing of

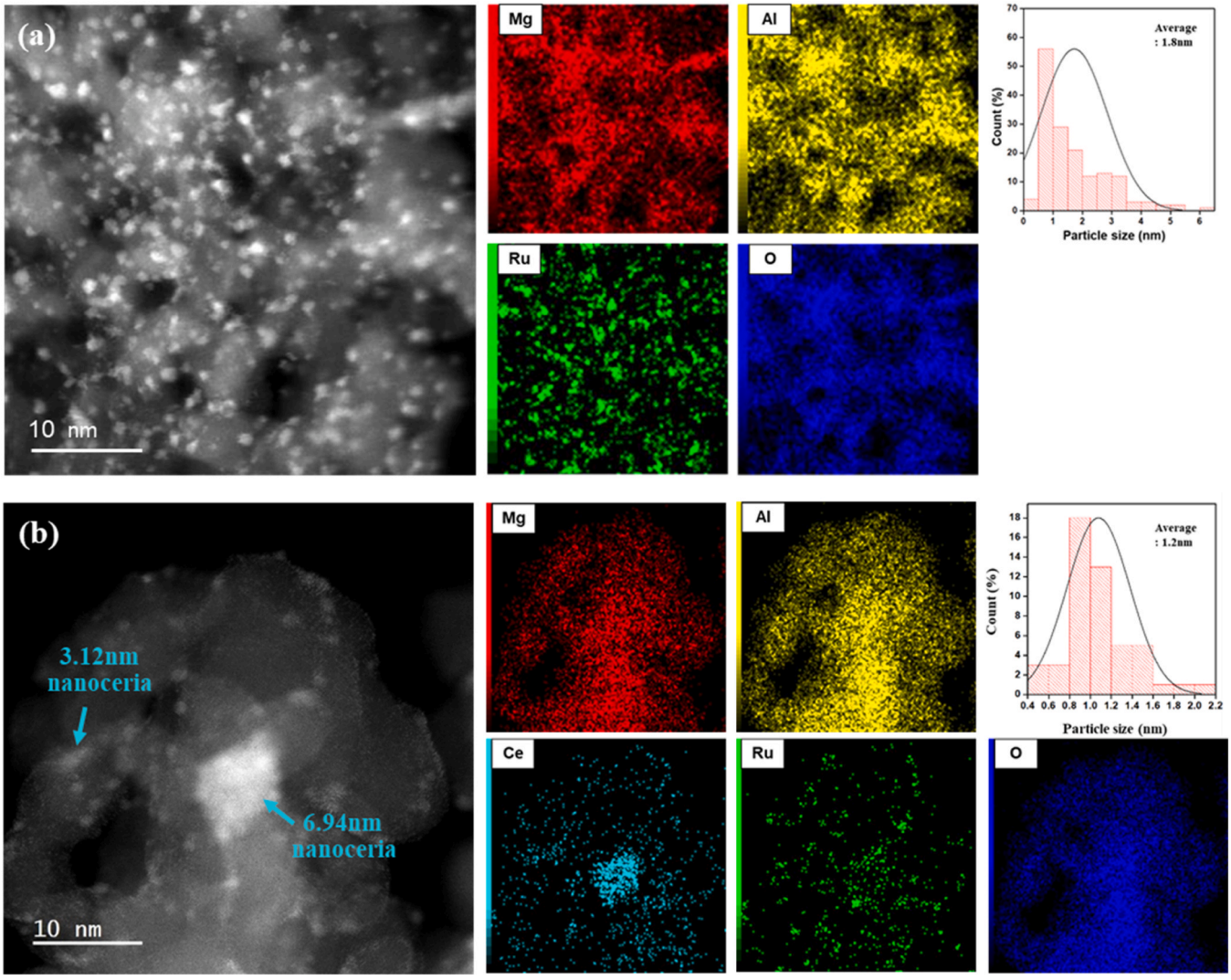

Fig. 3. STEM–EDS elemental mapping images with particle size distributions of the (a) Ru/MgAl and (b) Ru/Ce_5/$MgAl_{(600)}$ catalysts.

0.21 nm observed on the CeO_2 nanosheet surface corresponds to the (101) crystal plane of metallic Ru, indicating the presence of Ru NCs with a size of approximately 1.5 nm. In contrast, some individual bright spots corresponding to Ru atoms in Ru/Ce_5/$MgAl_{(600)}$ were observed near the amorphous CeO_2 on the MgAl surface and were assigned to be Ru single atoms (SAs). The amorphous support, which has a random atomic arrangement and diverse coordination environment, facilitates the formation of metal SAs [36,37]. Therefore, Ce addition improved Ru dispersion in the Ru/Ce_x/$MgAl_{(y00)}$ catalyst and induced a structure in which both Ru NCs and SAs coexist. Fig. S4 shows the HR-STEM images of the Ru/Ce_5/$MgAl_{(600)}$ catalysts after the ammonia decomposition reaction, and Ru NCs and SAs were still observed on the catalyst surface.

XPS was performed to characterize the interactions between Ru and CeO_2. The Ru valence states were determined from the Ru 3p profile, considering the overlapping C 1 s and Ru 3d peaks, and the results are shown in Fig. 5(a) and (b). Ru/MgAl exhibited a peak at 462.2 eV, which is attributed to Ru^0 [38,39]. As the CeO_2 content increased, a new peak emerged at a higher binding energy (464.8 eV), corresponding to the partially positively charged Ru ($Ru^{\delta+}$) species [38]. The $Ru^{\delta+}$ species refer to a state where the number of electrons is lower than that of the neutral state, which is related to the charge transfer associated with the formation of the $Ru^{\delta+}$-CeO_{2-x} interface [40,41]. The $Ru^{\delta+}$/Ru_{total} ratio in Ru/Ce_x/$MgAl_{(y00)}$ increased significantly from 8.69 % to 55.62 % with increasing Ce loading; however, a negligible change was observed when excess Ce (> 7.5 wt%) was added. Furthermore, as the Ce calcination temperature increased, the $Ru^{\delta+}$/Ru_{total} ratio decreased from 58.78 % to 40.69 %. Thus, the variation in the $Ru^{\delta+}$/Ru_{total} ratio was dependent on Ce addition, indicating that the chemical state of CeO_2 may influence the electronic interactions with Ru. The valence state of CeO_2 was derived from the Ce 3d profiles, as shown in Fig. 5(c) and (d). Catalysts containing CeO_2 are predominantly composed of Ce^{4+} and Ce^{3+}, whereas stoichiometric CeO_2, which is rich in oxygen, contains Ce^{4+}. Under reducing conditions, two electrons are released from the oxygen atoms in CeO_2 to form OVs. Subsequently, the electrons are transferred to two neighboring cerium ions, resulting in the conversion of Ce^{4+} to Ce^{3+}. In the deconvoluted Ce 3d spectra, the u and v peaks correspond to the $3d_{3/2}$ and $3d_{5/2}$ spin-orbit couplings, respectively. Peaks u_0, v_2, u_3, and v_3 represent Ce^{4+} (red lines), whereas peaks u_1 and v_1 represent Ce^{3+} (blue lines) [42,43]. For the Ru/Ce_x/$MgAl_{(y00)}$ catalysts, Ce^{3+} constituted a large fraction of 41.72–53.72 %, which was approximately 26.33–35.85 % higher than the Ce^{3+} fraction in the calcined Ce_x/$MgAl_{(y00)}$ catalysts, as shown in Figs. S5(a) and (b). The Ce^{3+} fraction is attributed to the OVs formed in CeO_2 under reducing conditions. In particular, the Ce^{3+} fraction decreased with increasing Ce loading and calcination temperature. Therefore, it is proposed that Ce addition affects OV formation. As shown in Figs. S5(c) and (d), the O 1 s XPS spectra for the Ce_x/$MgAl_{(y00)}$ catalysts were deconvoluted into three peaks. The 529.5–530.0 eV peak corresponded to lattice oxygen atoms

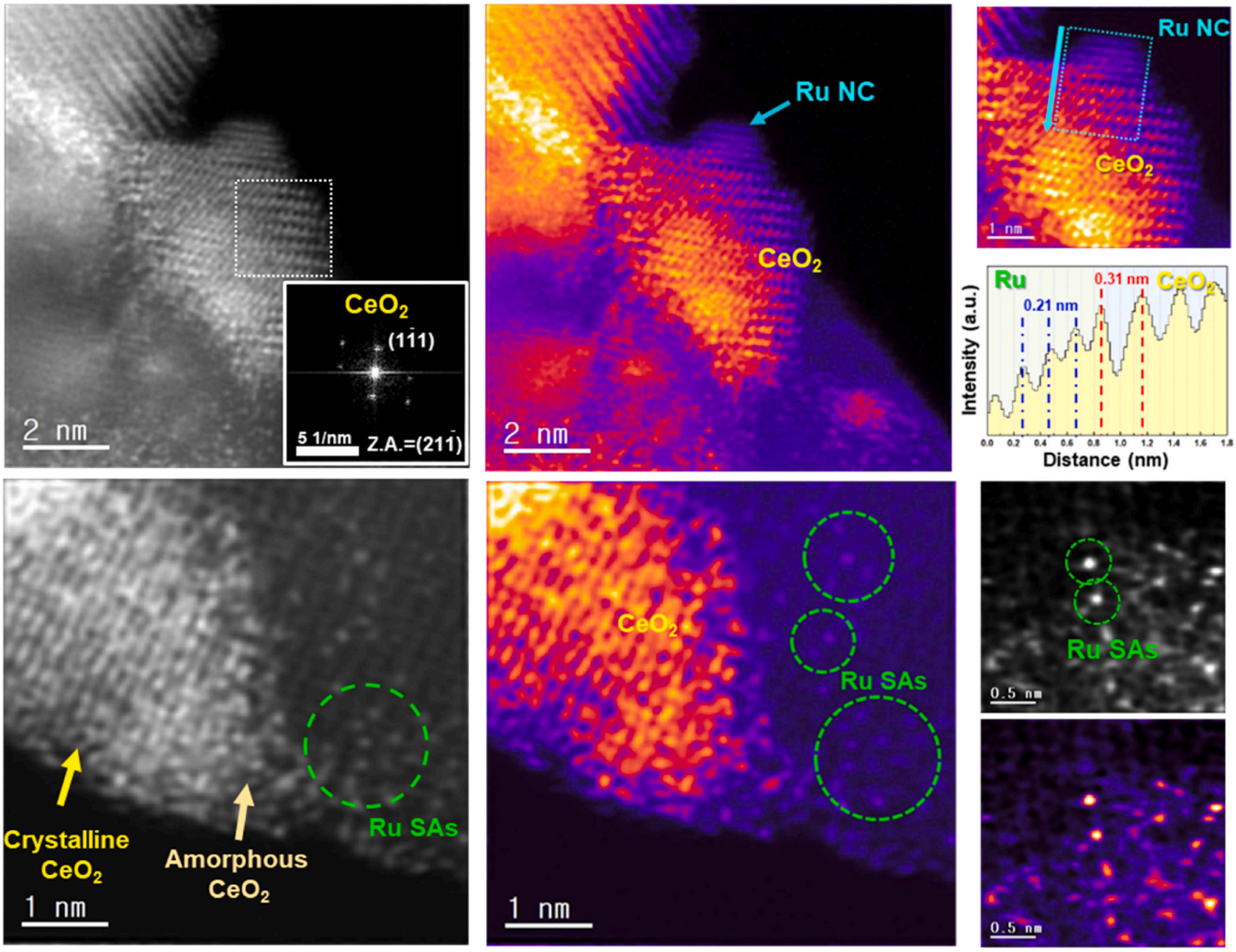

Fig. 4. HR-STEM images of the Ru/Ce_5/$MgAl_{(600)}$ catalysts.

O^{2-} (O_α), the 531.0–531.6 eV peak corresponded to surface adsorbed oxygen (O_β), and the 532.8–533.0 eV peak corresponded to hydroxyl-like species or chemisorbed water (O_γ) [44]. The O_β fraction is influenced by both the Ce loading and calcination temperature, suggesting that the abundant O_β species in Ce_x/$MgAl_{(y00)}$ affects OV formation.

The formation of OVs according to the Ce loading and calcination temperature can be understood based on the H_2 consumption of the Ce_x/$MgAl_{(y00)}$ catalysts, and the results are summarized in Table 1. The individual deconvoluted peaks derived from the H_2-TPR profiles shown in Fig. S6 were integrated to obtain H_2 consumption data (Supporting Information). As Ce loading increased, the total H_2 consumption increased from approximately 0.075 to 0.285 mmol·g^{-1}. However, when the Ce loading exceeded 5 wt%, the changes in H_2 consumption owing to surface oxygen species was negligible, whereas the consumption ratio of bulk/lattice oxygen species increased. Moreover, although there was almost no difference in the total H_2 consumption (0.101–0.104 mmol·g^{-1}) as the Ce calcination temperature increased, the H_2 consumption owing to surface oxygen species decreased from 0.104 to 0.077 mmol·g^{-1}. Fig. S7 shows the effect of OV formation in Ce_5/$MgAl_{(600)}$ on the ammonia decomposition performance compared to the performance of Ru/Ce_5/$MgAl_{(600)}$ reduced at different temperatures. A detailed discussion of these results is provided in the Supporting Information. Ru/Ce_5/$MgAl_{(600)}$ reduced at 600 °C exhibited excellent ammonia decomposition performance. This result indicates that the formation of OVs owing to the removal of surface oxygen from Ce_5/$MgAl_{(600)}$ plays a crucial role in enhancing the ammonia decomposition activity. The number of surface OVs originating from the H_2 consumption of Ce_x/$MgAl_{(y00)}$ was estimated, as listed in Table 1. The number of OVs increased from 0.013 to 0.051 when the Ce content was increased from 0 to 5 wt%. However, increasing the Ce content to above 7.5 wt% did not significantly change the amount of OVs. Furthermore, the amount of OVs in Ce_5/$MgAl_{(y00)}$ decreased from 0.052 to 0.039 mmol•g^{-1} with increasing calcination temperature.

The H_2-TPR profiles of the Ru/Ce_x/$MgAl_{(y00)}$ catalysts were obtained to evaluate the interactions between Ru and Ce, as shown in Fig. 6(a) and (b). The main peaks of Ru/MgAl were observed at 134 °C (peak I) and 265 °C (peak II). Typically, peak I corresponds to the reduction of the surface oxygen species of Ru on the MgAl surface, whereas peak II is related to the interaction between Ru and the support [45]. The increase in the Ce content resulted in more H_2 consumption below 300 °C. It is possible that the reduction peaks of the surface oxygen species for both the Ru species and the interacting CeO_2 overlap owing to the hydrogen spillover effect [46]. In particular, peak II clearly shifted to a lower temperature for the Ce-loaded catalyst, which may be owing to the formation of the Ru-Ce interface, which has superior redox properties [41]. The H_2-TPR results demonstrate that Ce addition causes a shift in peak II to a lower temperature, exhibiting a similar trend to the $Ru^{\delta+}$ fraction estimated using XPS, which was associated with a Ru-Ce interaction. Finally, the effects of surface OVs on the interaction

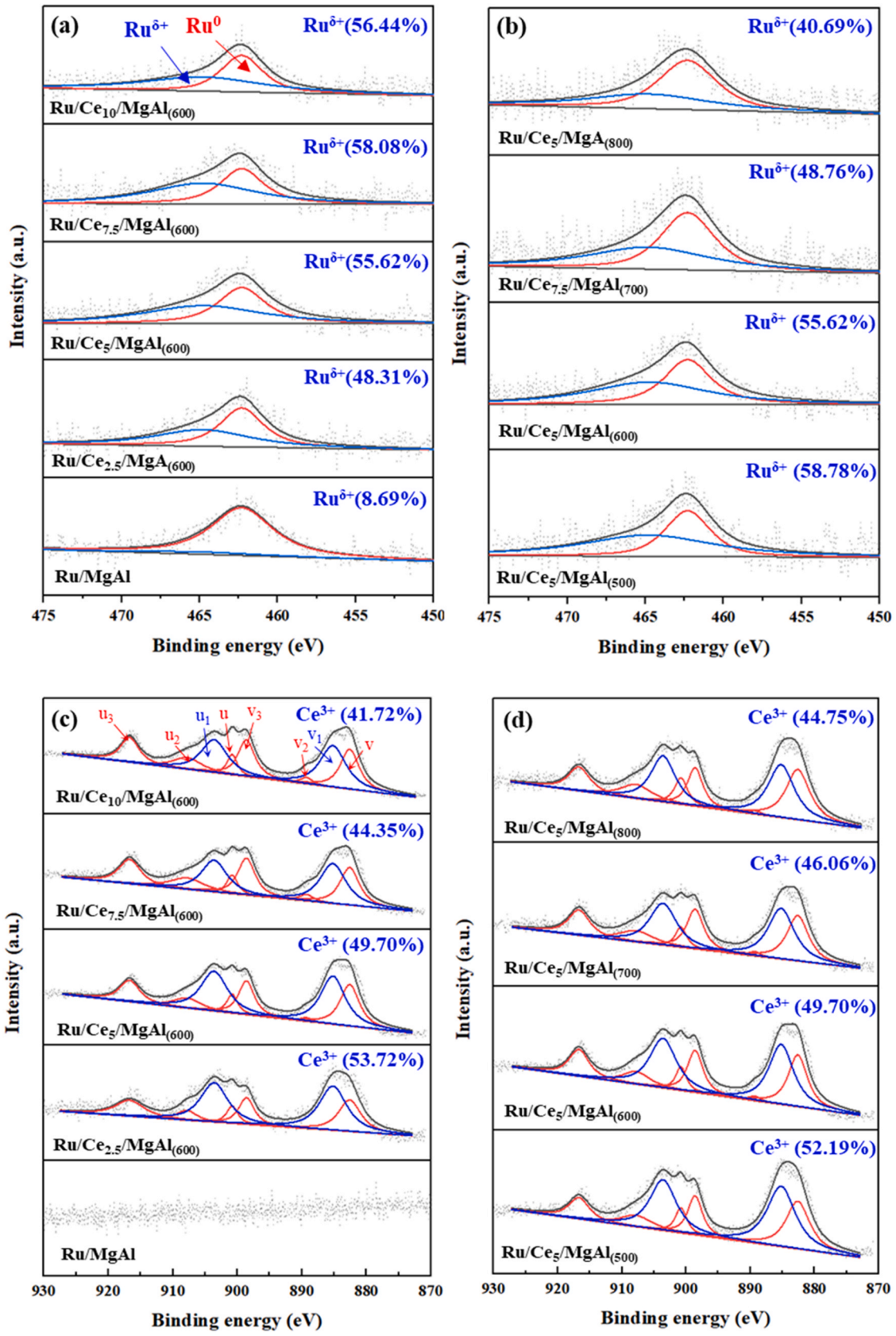

Fig. 5. Ru 3d XPS spectra with the $Ru^{\delta+}$ fractions of the $Ru/Ce_x/MgAl_{(y00)}$ catalysts as a function of (a) Ce loading and (b) Ce calcination temperature. Ce 3d XPS spectra with the Ce^{3+} fractions of the reduced $Ru/Ce_x/MgAl_{(y00)}$ catalysts as a function of (c) Ce loading and (d) Ce calcination temperature.

Table 1
H_2 consumption of surface and bulk/lattice oxygen species and O vacancies of the surface oxygen species in the $Ce_x/MgAl_{(y00)}$ catalysts.

	H_2-consumption (mmol•g^{-1})			O vacancies (mmol•g^{-1})
	Surface oxygen[1)]	Bulk/Lattice oxygen[2)]	Total[3)]	
MgAl	0.025	0.050	0.075	0.013
$Ce_{2.5}/MgAl_{(600)}$	0.080	0.064	0.143	0.040
$Ce_5/MgAl_{(600)}$	0.102	0.105	0.207	0.051
$Ce_{7.5}/MgAl_{(600)}$	0.106	0.140	0.246	0.053
$Ce_{10}/MgAl_{(600)}$	0.114	0.171	0.285	0.057
$Ce_5/MgAl_{(500)}$	0.104	0.097	0.201	0.052
$Ce_5/MgAl_{(700)}$	0.087	0.118	0.205	0.044
$Ce_5/MgAl_{(800)}$	0.077	0.129	0.206	0.039

1) H_2 consumption of surface oxygen species over Cex/MgAl(y00) (peak I + peak II).
2) H_2 consumption of bulk/lattice oxygen species over Cex/MgAl(y00) (peak III + peak IV).
3) Total = (H_2 consumption of surface oxygen species) + (H_2 consumption of bulk/lattice oxygen species).
4) O vacancies from surface oxygen species = (H_2 consumption of surface oxygen species) / 2.

between Ru and Ce, as well as on the ammonia decomposition performance were investigated, as shown in Fig. 6(c). The $Ru^{\delta+}$ fraction, which was estimated using XPS, increased linearly as the OV concentration increased from 0.013 to 0.057 mmol•g^{-1}. This clearly indicates that the interfacial Ru atoms possess significantly higher charge densities than the surface Ru atoms of Ru NCs. Additionally, the charge transfer from the surface OVs of ceria is much more facile in the interfacial layer, causing the interfacial Ru atoms to possess a highly oxidation state. Similarly, NH_3 conversion increased with increasing OV concentration and $Ru^{\delta+}$ fraction. Based on these results, it is concluded that changes in the Ce loading and calcination temperature influence the formation of surface OVs, which play a crucial role in enhancing the interaction between Ru and Ce as well as the ammonia decomposition activity.

Fig. S8 shows the Raman spectra of Ru/MgAl and $Ru/Ce_5/MgAl_{(600)}$ after pretreatment under reducing conditions. Although the CeO_2 content was insufficient to clearly detect the peaks, new peaks were observed at 460, 695, and 970 cm^{-1}. The 460 cm^{-1} peak corresponds to the fluorite $F_{2\,g}$ mode of CeO_2, whereas the 695 and 970 cm^{-1} peaks are attributed to electron-rich Ru species formed by strong interactions with CeO_2 [47]. CO_2-TPD analysis was performed to evaluate the distribution of basic sites in $Ru/Ce_x/MgAl_{(y00)}$, as presented in Fig. 7(a) and Table 2. The CO_2-TPD profile of Ru/MgAl exhibited peaks corresponding to weak and medium basic sites in the temperature ranges of < 170 °C and 170–320 °C, respectively. With an increase in Ce content, an additional peak corresponding to strong basic sites was observed at temperatures of > 320 °C. According to previous studies, weak basic sites are induced by OH groups, whereas medium and strong basic sites are induced by metal-oxygen pairs and low-coordination oxygen anions, respectively [48]. As listed in Table 2, the percentage of medium and strong basic sites, which are thought to be induced by oxygen deficiencies in Ru/MgAl, was 59.29 % of the total basic sites. However, this percentage increased to 65.76–73.75 % with increasing Ce content. Moreover, the percentage of strong basic sites, which was not observed in Ru/MgAl, increased significantly (up to 32.12 %) owing to Ce addition. This may be attributed to the basic sites induced by OVs on the CeO_2 surface interacting with Ru species [49].

The strength of CO chemical adsorption on the Ru species in the $Ru/Ce_x/MgAl_{(y00)}$ catalysts is closely related to the electron density, which depends on the electronic interactions between the metals and the reducible oxides. Therefore, in situ DRIFTS analysis for CO adsorption was performed at 50 °C. As shown in Fig. S9 and Table S3, for CO adsorption on Ru/MgAl, the peak at 2050 cm^{-1} corresponded to linear CO adsorbed on the Ru NCs (Ru^0-CO), whereas the peak at 1980 cm^{-1} corresponded to bridging CO ($2Ru^0$-CO) and/or linearly bonded CO on the Ru-top site [50]. As the Ce content increased, peaks were observed at 2066 and 1990 cm^{-1}, with a new peak appearing at 2120 cm^{-1}. The latter peak may be attributed to monocarbonyl or multicarbonyl species adsorbed on the $Ru^{\delta+}$ species with the oxygen-deficient site on the Ce surface[50]. The 2050 cm^{-1} peak blue-shifted to 2066 cm^{-1} and exhibited an increase in intensity, which is thought to be due to increased CO coverage on well-dispersed Ru^0 or the formation of new $Ru^{\delta+}$-$(CO)_x$ species via Ru-Ce interactions [51,52]. Therefore, it was determined that the 2066 cm^{-1} peak overlapped the peaks corresponding to $Ru^{\delta+}$-$(CO)_x$ and Ru^0-CO. Furthermore, the low-frequency peak observed at 1990 cm^{-1} corresponds to both carbonyl species

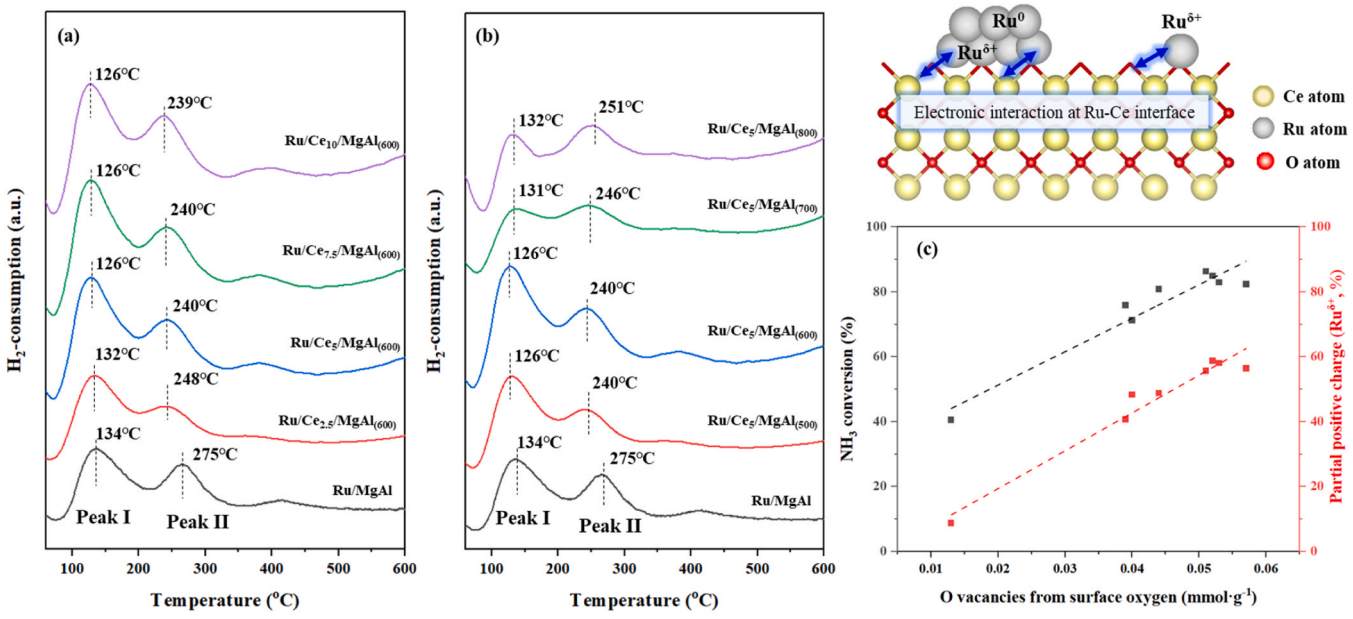

Fig. 6. H_2 consumption profiles based on the Ru-Ce interactions in the $Ru/Ce_5/MgAl_{(600)}$ catalysts as a function of (a) Ce loading and (b) Ce calcination temperature. (c) The correlation between the O vacancy concentration of surface oxygen species and the electron-deficient Ru species for ammonia decomposition.

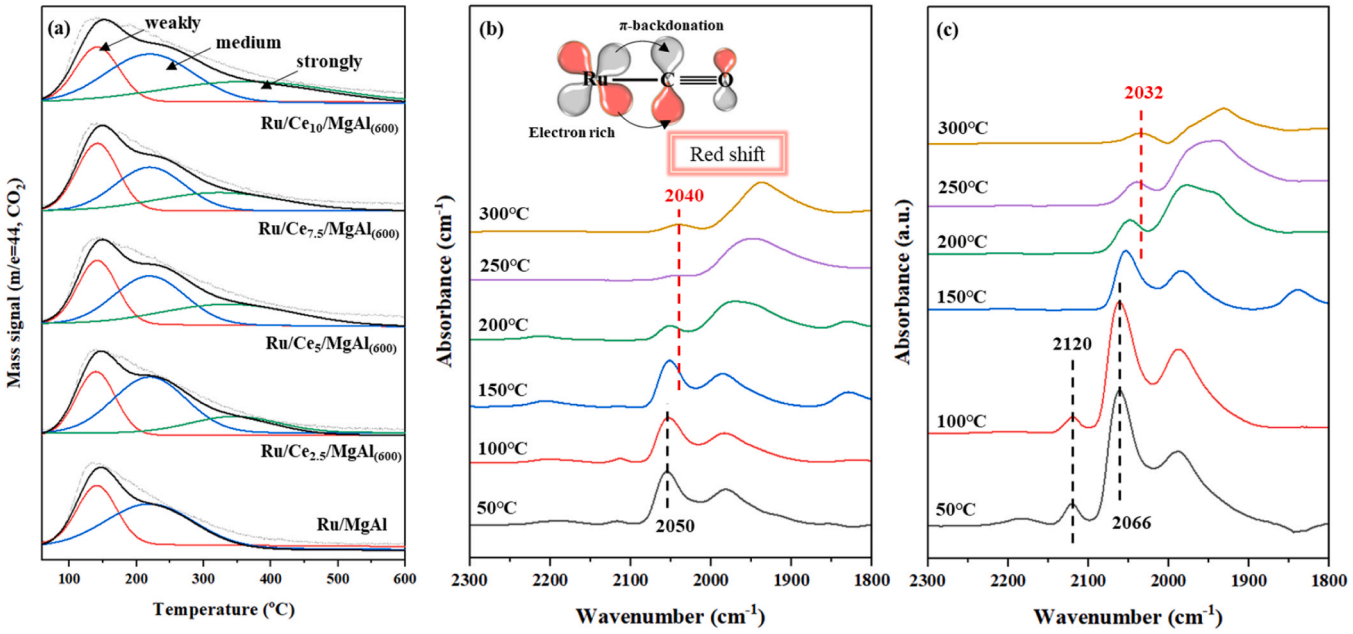

Fig. 7. (a) CO_2-TPD profiles of the Ru/Ce_x/$MgAl_{(600)}$ catalysts as a function of Ce loading. Temperature-dependent in situ CO-DRIFTS spectra, measured under He purging, of the (b) Ru/MgAl and (c) Ru/Ce_5/$MgAl_{(600)}$ catalysts preadsorbed with 10 % CO/He at 25 °C.

Table 2
The contribution of basicity in the Ru/Ce_x/$MgAl_{(y00)}$ catalysts determined by CO_2-TPD analysis.

	CO_2 desorbed area (%)			
	Weak	Medium	Strong	Medium + strong
Ru/MgAl	40.71	59.29	-	59.29
Ru/$Ce_{2.5}$/$MgAl_{(600)}$	33.11	49.03	17.86	66.89
Ru/Ce_5/$MgAl_{(600)}$	28.80	39.36	31.84	71.20
Ru/$Ce_{7.5}$/$MgAl_{(600)}$	29.50	39.13	31.37	70.50
Ru/Ce_{10}/$MgAl_{(600)}$	26.25	41.63	32.12	73.75
Ru/Ce_5/$MgAl_{(500)}$	30.15	42.85	27.00	69.85
Ru/Ce_5/$MgAl_{(700)}$	31.16	42.33	26.51	68.84
Ru/Ce_5/$MgAl_{(800)}$	34.24	44.81	20.95	65.76

adsorbed on Ru^0 and linearly bonded carbonyl species adsorbed on $Ru^{\delta+}$ [53]. Based on the CO adsorption on the Ru/MgAl and Ru/Ce_x/$MgAl_{(y00)}$ catalysts at 50 °C, the CO adsorption/desorption behavior of the Ru species was compared by heating the catalysts to 300 °C under He gas flow. The peak observed at 2050 cm^{-1} in the Ru/MgAl catalyst was gradually red-shifted at temperatures above 200 °C, eventually shifting to 2040 cm^{-1} (Fig. 7(b)). In the DRIFTS profile of Ru/Ce_5/$MgAl_{(600)}$ shown in Fig. 7(c), the peak at 2066 cm^{-1} shifted to 2032 cm^{-1}, indicating a significantly stronger redshift than that of Ru/MgAl. A red-shift is observed when π-back-donation from a noble metal with abundant electrons occurs to form CO antibonding orbitals, which results in strongly adsorbed CO [50,54–56]. In contrast, the peak observed at 2120 cm^{-1}, which is owing to CO adsorption on $Ru^{\delta+}$ in Ru/Ce_5/$MgAl_{(600)}$, represents a weak bonding characteristic. This peak disappeared completely at 150 °C, indicating a weak interaction with CO. The area of the 2066 cm^{-1} peak sharply decreased at 150 °C, which is thought to be related to the desorption of $Ru^{\delta+}$-$(CO)_x$. These results demonstrate that CeO_2 addition increases the surface electron density of the Ru^0 on the Ru NCs via electron transfer.

3.3. Ammonia decomposition behavior

The influence of the physicochemical properties of the catalysts on ammonia decomposition was analyzed. The desorption behaviors of NH_3, N_2, and H_2 from the catalysts with different Ce contents were analyzed by NH_3-TPD as a function of temperature, as shown in Fig. 8. Fig. 8(a) shows the NH_3 desorption intensities of Ru/MgAl at < 150, 150–280, and > 280 °C, which correspond to the weak, medium, and strong acid sites of MgAl, respectively [57]. Ce addition resulted in a decrease in the strong acid sites of MgAl, whereas the peak related to medium acid sites observed at 215 °C shifted to 196 °C and the peak intensity increased. This peak shift to a lower temperature indicates a weaker NH_3 binding strength, which is associated with NH_3 adsorbed on the Lewis acid sites of the OVs in CeO_2 [58]. The mass profiles of N_2 and H_2 desorbed from ammonia adsorbed on the Ru sites are shown in Figs. 8 (b) and 8(c), respectively. The desorption of N_2 and H_2 from Ru/MgAl was observed at approximately 300 and 305 °C, respectively. This indicates that the dissociation of ammonia and recombination/desorption of N and H are complete at temperatures below 305 °C. Ce addition resulted in a decrease in the temperature required for N_2 and H_2 desorption, and the desorption peaks shifted to lower temperatures of approximately 260 and 265 °C, respectively. It is evident that Ce addition facilitates the recombination/desorption of N_2 and H_2 atoms at lower temperatures in addition to NH_3 dissociation, which results in enhanced reaction activity. Notably, the N_2 recombination and desorption steps are well-known RDSs for Ru-based catalysts. However, the effects of H_2 desorption have rarely been reported thus far.

In situ NH_3-DRIFTS analysis was performed to evaluate the ammonia decomposition behavior of the Ru/MgAl and Ru/Ce_5/$MgAl_{(600)}$ catalysts, and the results are shown in Fig. 9. The samples were treated in a 10 % NH_3/He atmosphere at 50 °C for approximately 30 min, and then in situ NH_3-DRIFTS analysis was performed after desorption with He in the temperature range of 50–300 °C. In the profiles obtained at 50 °C intervals, peaks corresponding to adsorbed ammonia and intermediate species on the catalyst surface were observed in the ranges of 4000–2500 and 2000–800 cm^{-1}, respectively. The peaks observed at 3370, 3268, and 1618 cm^{-1} for both catalysts were associated with ammonia adsorbed on Lewis acid sites. The peaks in the range of 3400–3150 cm^{-1} mainly corresponded to N-H stretching vibrations, whereas the peak at 1618 cm^{-1} was attributed to asymmetric deformation modes [59,60]. The peaks at 1421–1439 and 1180–1197 cm^{-1} corresponded to the -NH deformation mode and amide (-NH_2) rocking from NH_3 dissociation, respectively [60,61]. In particular, the temperature required for the removal of NH_x species from the surfaces of

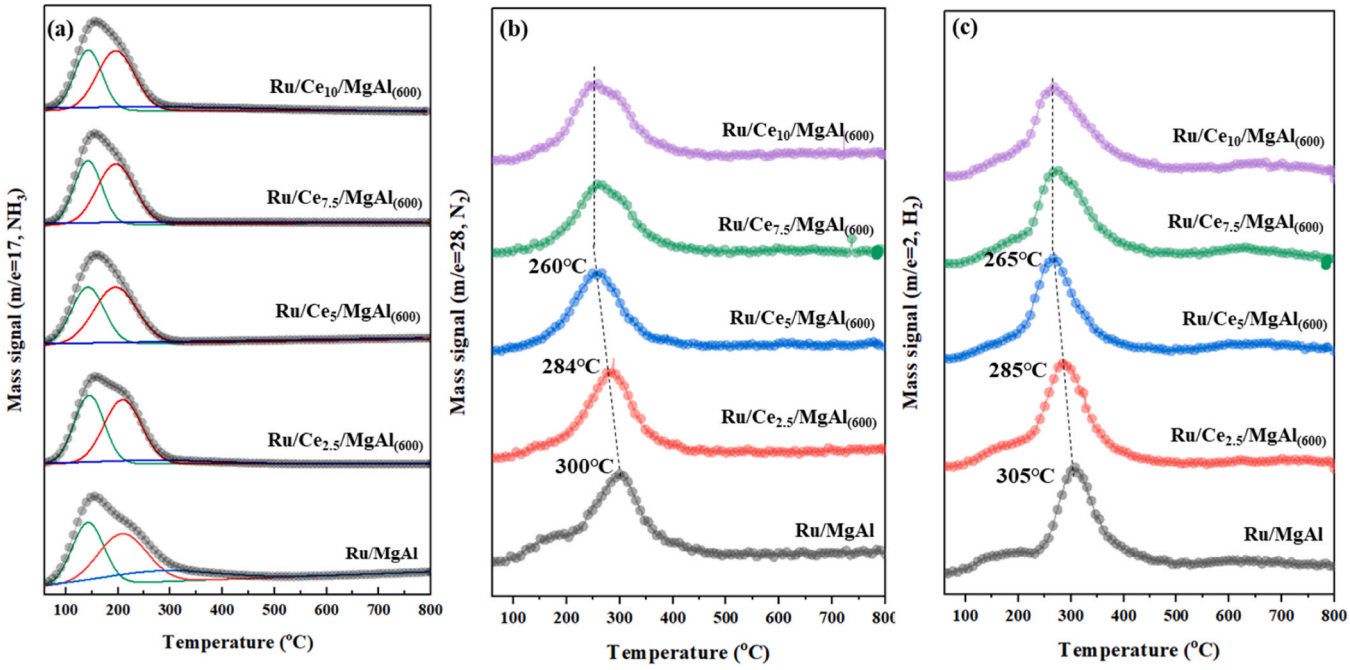

Fig. 8. NH_3-TPD profiles of (a) NH_3 (m/e=17), (b) N_2 (m/e=28) and (c) H_2 (m/e=2) over the $Ru/Ce_x/MgAl_{(600)}$ catalysts as a function of Ce loading.

Ru/MgAl and $Ru/Ce_5/MgAl_{(600)}$ shifted from approximately 250° to 200°C, which indicates the improved dissociation ability owing to CeO_2. In addition, a peak was observed at 1809 cm^{-1} corresponding to the presence of hydrides (Ru^0-H) adsorbed on top of the Ru metal particles, along with a decrease in the peak intensity of the NH_x species [24]. This indicates that the dissociation of the NH_x species likely occurs on the Ru NC surface. One of the proposed RDSs for the ammonia decomposition reaction is the formation of NH_x and H atoms via NH_3 dissociation. However, the removal temperatures of the NH_x species do not correspond to the desorption temperatures of N_2 and H_2 observed in the NH_3-TPD profile (Fig. 8). This indicated that the recombination/desorption of N and H on the Ru surface corresponds to the RDS of the catalyst. In fact, the temperatures required for complete removal of the Ru^0-H peak (1809 cm^{-1}) on the surfaces of both catalysts were different. The complete removal of Ru^0-H on the Ru/MgAl surface occurred at approximately 300 °C, whereas it shifted to a lower temperature of approximately 250 °C on the $Ru/Ce_5/MgAl_{(600)}$ surface. According to previously reported literature [62,63], ammonia synthesis/decomposition catalysts can be inhibited by H_2 poisoning, and H_2 migration can contribute to improving catalyst performance by accelerating reaction cycles on the active site. A nonreducible MgAl support forms more OVs from the added CeO_2, which accelerates the transfer of H atoms from the metal to the support via the hydrogen spillover effect [64]. Li et al. [65] reported that abundant oxygen defects causes a strong interaction between Ru and Ce, which significantly affects the migration and desorption of hydrogen species as well as nitrogen activation in ammonia synthesis. Cao et al. [66] reported that catalysts should weakly bond with H atoms to achieve rapid H_2 desorption, and that partially positively charged $Ru^{\delta+}$ promotes H_2 desorption by significantly weakening the Ru-H bond strength compared with metallic Ru. Therefore, it is proposed that $Ru^{\delta+}$ at the interface between Ru and CeO_2 serves as a recombination/desorption site for migrated H atoms. Furthermore, the desorption of N atoms was observed by NH_3-TPD analysis, although it was not observed by DRIFTs analysis. The enhanced electron-donating properties of the Ru NCs are known to accelerate the recombination/desorption rates of N atoms during ammonia decomposition [17–19]. Therefore, this study proposes a catalyst for ammonia decomposition by introducing CeO_2 with abundant surface OVs, which facilitate the rapid removal of N atoms sequestered in Ru NCs, while simultaneously providing a novel pathway for the recombination of H atoms.

4. Conclusion

This study investigated the effect of CeO_2 with abundant surface OVs in $Ru/Ce_x/MgAl_{(y00)}$ catalysts on ammonia decomposition. H_2-TPR analysis revealed that CeO_2 enhanced the oxygen storage capacity of the MgAl support and provided abundant surface OVs under reducing conditions. The morphology of Ru was characterized by HR-STEM, which revealed well-dispersed Ru NCs and SAs on the surfaces of hemispherical and amorphous CeO_2. Based on XPS analysis, the $Ru/Ce_x/MgAl_{(y00)}$ catalysts contained metallic Ru (Ru^0) species and partially positively charged Ru ($Ru^{\delta+}$) species, which was formed by the electronic interactions of Ru with the surface OVs at the Ru-Ce interface. The $Ru^{\delta+}$ fraction increased linearly with surface OV concentration, which was controlled by the Ce loading and calcination temperature. CO_2-TPD and in situ CO-DRIFTS analyses indicated that the abundant surface OVs of CeO_2 increased its basicity and demonstrated the superior electron-donating properties of the dispersed Ru NCs. NH_3-TPD and in situ NH_3-DRIFTS analyses revealed that the recombination/desorption of N and H atoms was the RDS. The enhanced electron-donating properties of Ru NCs accelerated the recombination and desorption of N atoms. Furthermore, the hydrogen spillover effect rapidly removed H atoms from metallic Ru and $Ru^{\delta+}$ served as a recombination/desorption site for spillover H atoms. Compared to Ru/MgAl, the optimized $Ru/Ce_5/MgAl_{(600)}$ catalyst exhibited a significantly improved ammonia decomposition activity at low temperatures (below 500 °C) and maintained an equivalent performance at an approximately eight times higher WHSV. Additionally, $Ru/Ce_5/MgAl_{(600)}$ demonstrated a high H_2 formation rate (27.4 $mmol_{H2}{\cdot}g_{cat}^{-1}{\bullet}min^{-1}$ at 30,000 $mL{\cdot}g_{cat}^{-1}{\cdot}h^{-1}$, 450 °C) compared to previously reported ammonia decomposition catalysts. Long-term stability testing confirmed that $Ru/Ce_5/MgAl_{(600)}$ not only exhibits a stable ammonia decomposition performance at 450 °C but also maintains thermal durability after aging at 650 °C. Therefore, this study provides insight into the role of CeO_2 on the physicochemical properties and ammonia decomposition performance of the Ru-based catalysts. Furthermore, the facile catalyst synthesis process can contribute to the design of practical catalysts for CO_x-free H_2 production.

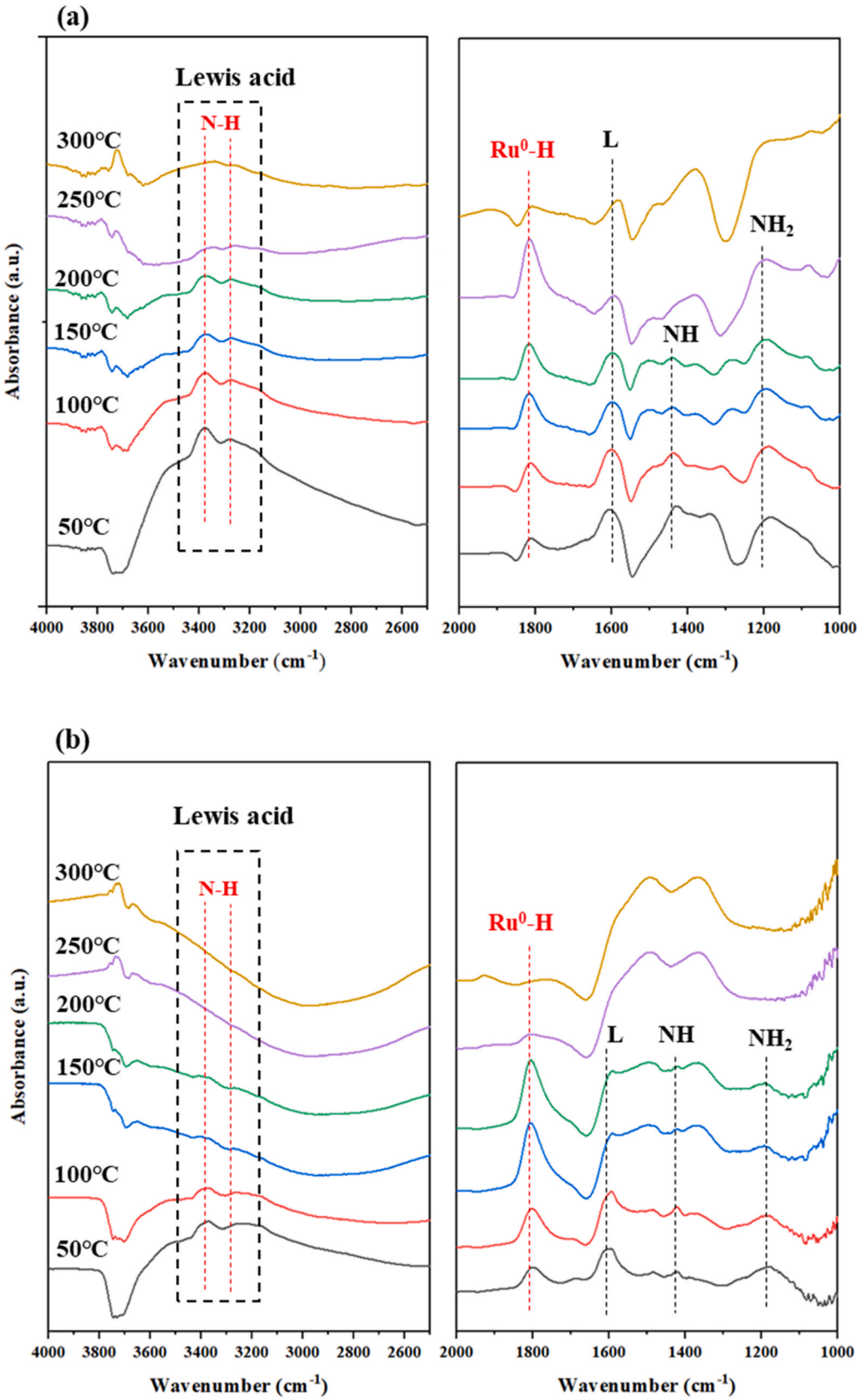

Fig. 9. In situ DRIFTS measured under He purging and various temperatures for the 10 % NH_3 preadsorbed (a) Ru/MgAl and (b) $Ru/Ce_5/MgAl_{(600)}$ catalysts.

CRediT authorship contribution statement

JungHun Shin: Conceptualization, Validation, Data curation, Writing – original draft. **Unho Jung:** Project administration, Writing – review & editing. **Jiyu Kim:** Performed the experiments, refined and interpreted the data. **Kyoung Deok Kim:** Performed the experiments. **Dahye Song:** Performed the analysis. **Yongha Park:** Validation, Writing – review & editing. **Byeong-seon An:** Performed and interpreted the TEM analysis. **Kee Young Koo:** Supervision, Validation, Writing – review & editing.

Declaration of Competing Interest

The authors declare that they have no known competing financial interests or personal relationships that could have appeared to influence the work reported in this paper.

Data availability

The authors do not have permission to share data.

Acknowledgements

This study was supported by the Ministry of Trade, Industry & Energy (MOTIE) and the Korea Institute of Energy Technology Evaluation and Planning (KETEP) of the Republic of Korea (Grant no. 20213030040550).

Appendix A. Supporting information

Supplementary data associated with this article can be found in the online version at doi:10.1016/j.apcatb.2023.123234.

References

[1] A. Midilli, I. Dincer, Hydrogen as a renewable and sustainable solution in reducing global fossil fuel consumption, Int. J. Hydrog. Energy 33 (2008) 4209–4222, https://doi.org/10.1016/j.ijhydene.2008.05.024.
[2] K. Klöckner, P. Letmathe, Is the coherence of coal phase-out and electrolytic hydrogen production the golden path to effective decarbonisation, Appl. Energy 279 (2020), 115779, https://doi.org/10.1016/j.apenergy.2020.115779.
[3] D. Parra, L. Valverde, F.J. Pino, M.K. Patel, A review on the role, cost and value of hydrogen energy systems for deep decarbonisation, Renew. Sustain. Energy Rev. 101 (2019) 279–294, https://doi.org/10.1016/j.rser.2018.11.010.
[4] F. Schüth, R. Palkovits, R. Schlögl, D.S. Su, Ammonia as a possible element in an energy infrastructure: catalysts for ammonia decomposition, Energy Environ. Sci. 5 (2012) 6278–6289, https://doi.org/10.1039/C2EE02865D.
[5] J. Guo, P. Chen, Catalyst: NH_3 as an energy carrier, Chem 3 (2017) 709–712, https://doi.org/10.1016/j.chempr.2017.10.004.
[6] A.T. Wijayanta, T. Oda, C.W. Purnomo, T. Kashiwagi, M. Aziz, Liquid hydrogen, methylcyclohexane, and ammonia as potential hydrogen storage: comparison review, Int. J. Hydrog. Energy 44 (2019) 15026–15044, https://doi.org/10.1016/j.ijhydene.2019.04.112.
[7] Y. Im, H. Muroyama, T. Matsui, K. Eguchi, Ammonia decomposition over nickel catalysts supported on alkaline earth metal aluminate for H_2 production, Int. J. Hydrog. Energy 45 (2020) 26979–26988, https://doi.org/10.1016/j.ijhydene.2020.07.014.
[8] J.C. Ganley, F. Thomas, E. Seebauer, R.I. Masel, A priori catalytic activity correlations: the difficult case of hydrogen production from ammonia, Catal. Lett. 96 (2004) 117–122, https://doi.org/10.1023/B:CATL.0000030108.50691.d4.
[9] C. Chen, K. Wu, H. Ren, C. Zhou, Y. Luo, L. Lin, C. Au, L. Jiang, Ru-based catalysts for ammonia decomposition: a mini-review, Energy Fuels 35 (2021) 11693–11706, https://doi.org/10.1021/acs.energyfuels.1c01261.
[10] A.K. Hill, L. Torrente-Murciano, Low temperature H_2 production from ammonia using ruthenium-based catalysts: synergetic effect of promoter and support, Appl. Catal. B-Environ. 172 (2015) 129–135, https://doi.org/10.1016/j.apcatb.2015.02.011.
[11] S. Yin, B. Xu, W. Zhu, C. Ng, X. Zhou, C. Au, Carbon nanotubes-supported Ru catalyst for the generation of COx-free hydrogen from ammonia, Catal. Today 93 (2004) 27–38, https://doi.org/10.1016/j.cattod.2004.05.011.
[12] J. Chen, Z.H. Zhu, S. Wang, Q. Ma, V. Rudolph, G.Q. Lu, Effects of nitrogen doping on the structure of carbon nanotubes (CNTs) and activity of Ru/CNTs in ammonia decomposition, Chem. Eng. J. 156 (2010) 404–410, https://doi.org/10.1016/j.cej.2009.10.062.
[13] A.M. Karim, V. Prasad, G. Mpourmpakis, W.W. Lonergan, A.I. Frenkel, J.G. Chen, D.G. Vlachos, Correlating particle size and shape of supported Ru/γ-Al_2O_3 catalysts with NH3 decomposition activity, J. Am. Chem. Soc. 131 (2009) 12230–12239, https://doi.org/10.1021/ja902587k.
[14] C. Huang, Y. Yu, J. Yang, Y. Yan, D. Wang, F. Hu, X. Wang, R. Zhang, G. Feng, Ru/La_2O_3 catalyst for ammonia decomposition to hydrogen, Appl. Surf. Sci. 476 (2019) 928–936, https://doi.org/10.1016/j.apsusc.2019.01.112.
[15] X. Ju, L. Liu, X. Zhang, J. Feng, T. He, P. Chen, Highly efficient Ru/MgO catalyst with surface-enriched basic sites for production of hydrogen from ammonia decomposition, ChemCatChem 11 (2019) 4161–4170, https://doi.org/10.1002/cctc.201900306.
[16] X. Ju, L. Liu, P. Yu, J. Guo, X. Zhang, T. He, G. Wu, P. Chen, Mesoporous Ru/MgO prepared by a deposition-precipitation method as highly active catalyst for producing COx-free hydrogen from ammonia decomposition, Appl. Catal. B Environ. 211 (2017) 167–175, https://doi.org/10.1016/j.apcatb.2017.04.043.
[17] S. Wang, S. Yin, L. Li, B. Xu, C. Ng, C. Au, Investigation on modification of Ru/CNTs catalyst for the generation of COx-free hydrogen from ammonia, Appl. Catal. B Environ. 52 (2004) 287–299, https://doi.org/10.1016/j.apcatb.2004.05.002.
[18] A.K. Hill, L. Torrente-Murciano, In-situ H_2 production via low temperature decomposition of ammonia: insights into the role of cesium as a promoter, Int. J. Hydrog. Energy 39 (2014) 7646–7654, https://doi.org/10.1016/j.ijhydene.2014.03.043.
[19] Z. Wang, Y. Qu, X. Shen, Z. Cai, Ruthenium catalyst supported on Ba modified ZrO2 for ammonia decomposition to COx-free hydrogen, Int. J. Hydrog. Energy 44 (2019) 7300–7307, https://doi.org/10.1016/j.ijhydene.2019.01.235.
[20] B. Lin, Y. Liu, L. Heng, X. Wang, J. Ni, J. Lin, L. Jiang, Morphology effect of ceria on the catalytic performances of Ru/CeO_2 catalysts for ammonia synthesis, Ind. Eng. Chem. Res. 57 (2018) 9127–9135, https://doi.org/10.1021/acs.iecr.8b02126.
[21] M. Nolan, S.C. Parker, G.W. Watson, The electronic structure of oxygen vacancy defects at the low index surfaces of ceria, Surf. Sci. 595 (2005) 223–232, https://doi.org/10.1016/j.susc.2005.08.015.
[22] Y. Li, L. Wu, Y. Wang, P. Ke, J. Xu, B. Guan, γ-Al_2O_3 doped with cerium to enhance electron transfer in catalytic ozonation of phenol, J. Water Process. Eng. 36 (2020), 101313, https://doi.org/10.1016/j.jwpe.2020.101313.
[23] W. Li, Z. Qiang, T. Zhang, F. Cao, Kinetics and mechanism of pyruvic acid degradation by ozone in the presence of PdO/CeO_2, Appl. Catal. B Environ. 113 (2012) 290–295, https://doi.org/10.1016/j.apcatb.2011.11.049.
[24] X.-C. Hu, X.-P. Fu, W.-W. Wang, X. Wang, K. Wu, R. Si, C. Ma, C.-J. Jia, C.-H. Yan, Ceria-supported ruthenium clusters transforming from isolated single atoms for hydrogen production via decomposition of ammonia, Appl. Catal. B Environ. 268 (2020), 118424, https://doi.org/10.1016/j.apcatb.2019.118424.
[25] T.A. Le, Y. Kim, H.W. Kim, S.-U. Lee, J.-R. Kim, T.-W. Kim, Y.-J. Lee, H.-J. Chae, Ru-supported lanthania-ceria composite as an efficient catalyst for COx-free H_2 production from ammonia decomposition, Appl. Catal. B Environ. 285 (2021), 119831, https://doi.org/10.1016/j.apcatb.2020.119831.
[26] D. Song, U. Jung, H.B. Im, T.H. Lee, Y.-E. Kim, K.B. Lee, K.Y. Koo, Comparison of preparation methods for improving coke resistance of Ni-Ru/$MgAl_2O_4$ catalysts in dry reforming of methane for syngas production, Energy Sources A Recovery Util. Environ. Eff. 44 (2022) 10755–10765, https://doi.org/10.1080/15567036.2021.1994669.
[27] Z. Wang, Z. Cai, Z. Wei, Highly active ruthenium catalyst supported on barium hexaaluminate for ammonia decomposition to COx-Free hydrogen, ACS Sustain. Chem. Eng. 7 (2019) 8226–8235, https://doi.org/10.1021/acssuschemeng.8b06308.
[28] X. Zhang, L. Liu, J. Feng, X. Ju, J. Wang, T. He, P. Chen, Metal–support interaction-modulated catalytic activity of Ru nanoparticles on Sm_2O_3 for efficient ammonia decomposition, Catal. Sci. Technol. 11 (2021) 2915–2923, https://doi.org/10.1039/D1CY00080B.
[29] K. Yamazaki, M. Matsumoto, M. Ishikawa, A. Sato, NH_3 decomposition Over Ru/CeO_2-PrOx catalyst under high space velocity conditions for an on-site H_2 fueling station, Appl. Catal. B Environ. 325 (2022), 122352, https://doi.org/10.1016/j.apcatb.2022.122352.
[30] Q. Su, L. Gu, A. Zhong, Y. Yao, W. Ji, W. Ding, C. Au, Layered double hydroxide derived Mg_2Al-LDO supported and K-modified Ru catalyst for hydrogen production via ammonia decomposition, Catal. Lett. 148 (2018) 894–903, https://doi.org/10.1007/s10562-017-2195-1.
[31] F. Zhiqiang, W. Ziqing, L. Dexing, L. Jianxin, Y. Lingzhi, W. Qin, W. Zhong, Catalytic ammonia decomposition to COx-free hydrogen over ruthenium catalyst supported on alkali silicates, Fuel 326 (2022), 125094, https://doi.org/10.1016/j.fuel.2022.125094.
[32] K.E. Lamb, M.D. Dolan, D.F. Kennedy, Ammonia for hydrogen storage; a review of catalytic ammonia decomposition and hydrogen separation and purification, Int. J. Hydrog. Energy 44 (2019) 3580–3593, https://doi.org/10.1016/j.ijhydene.2018.12.024.
[33] J. Yu, Y. Dai, X. Wu, Z. Zhang, Q. He, C. Cheng, Z. Wu, Z. Shao, M. Ni, Ultrafine ruthenium-iridium alloy nanoparticles well-dispersed on N-rich carbon frameworks as efficient hydrogen-generation electrocatalysts, Chem. Eng. J. 417 (2021), 128105, https://doi.org/10.1016/j.cej.2020.128105.
[34] S.M. Lee, H.H. Lee, S.C. Hong, Influence of calcination temperature on Ce/TiO_2 catalysis of selective catalytic oxidation of NH_3 to N_2, Appl. Catal. A Gen. 470 (2014) 189–198, https://doi.org/10.1016/j.apcata.2013.10.057.
[35] A. Trovarelli, C. Deleitenburg, G. Dolcetti, J. Lorca, CO_2 methanation under transient and steady-state conditions over Rh/CeO_2 and CeO_2-promoted Rh/SiO_2: the role of surface and bulk ceria, J. Catal. 151 (1995) 111–124, https://doi.org/10.1006/jcat.1995.1014.

[36] Y. Liu, X. Liu, A.R. Jadhav, T. Yang, Y. Hwang, H. Wang, L. Wang, Y. Luo, A. Kumar, J. Lee, Unraveling the function of metal–amorphous support interactions in single-atom electrocatalytic hydrogen evolution, Angew. Chem. Int. Ed. 61 (2020), e202114160, https://doi.org/10.1002/anie.202114160.
[37] Y. Hu, G. Luo, L. Wang, X. Liu, Y. Qu, Y. Zhou, F. Zhou, Z. Li, Y. Li, T. Yao, Single Ru atoms stabilized by hybrid amorphous/crystalline FeCoNi layered double hydroxide for ultraefficient oxygen evolution, Adv. Energy Mater. 11 (2021), 2002816, https://doi.org/10.1002/aenm.202002816.
[38] X. Wang, G. Lan, H. Liu, Y. Zhu, Y. Li, Effect of acidity and ruthenium species on catalytic performance of ruthenium catalysts for acetylene hydrochlorination, Catal. Sci. Technol. 8 (2018) 6143–6149, https://doi.org/10.1039/C8CY01677A.
[39] Z.-F. Zhao, Z.-J. Wu, L.-X. Zhou, M.-H. Zhang, W. Li, K.-Y. Tao, Synthesis of a nano-nickel catalyst modified by ruthenium for hydrogenation and hydrodechlorination, Catal. Commun. 9 (2008) 2191–2194, https://doi.org/10.1016/j.catcom.2008.04.018.
[40] Z. Liu, F. Zhang, N. Rui, X. Li, L. Lin, L.E. Betancourt, D. Su, W. Xu, J. Cen, K. Attenkofer, Highly active ceria-supported Ru catalyst for the dry reforming of methane: In situ identification of $Ru^{\delta+}$–Ce^{3+} interactions for enhanced conversion, ACS Catal. 9 (2019) 3349–3359, https://doi.org/10.1021/acscatal.8b05162.
[41] Y. Guo, S. Mei, K. Yuan, D.-J. Wang, H.-C. Liu, C.-H. Yan, Y.-W. Zhang, Low-temperature CO_2 methanation over CeO_2-supported Ru single atoms, nanoclusters, and nanoparticles competitively tuned by strong metal–support interactions and H-spillover effect, ACS Catal. 8 (2018) 6203–6215, https://doi.org/10.1021/acscatal.7b04469.
[42] T. Xia, S. Yao, Z. Wu, G. Li, J. Li, High ratio of Ce^{3+}/(Ce^{3+}+ Ce^{4+}) enhanced the plasma catalytic degradation of n-undecane on CeO_2/γ-Al_2O_3, J. Hazard. Mater. 424 (2022), 127700, https://doi.org/10.1016/j.jhazmat.2021.127700.
[43] Y. Li, X. Wang, C. Song, Spectroscopic characterization and catalytic activity of Rh supported on CeO_2-modified Al_2O_3 for low-temperature steam reforming of propane, Catal. Today 263 (2016) 22–34, https://doi.org/10.1016/j.cattod.2015.08.063.
[44] W. Zhao, Y. Tang, Y. Wan, L. Li, S. Yao, X. Li, J. Gu, Y. Li, J. Shi, Promotion effects of SiO_2 or/and Al_2O_3 doped CeO_2/TiO_2 catalysts for selective catalytic reduction of NO by NH_3, J. Hazard. Mater. 278 (2014) 350–359, https://doi.org/10.1016/j.jhazmat.2014.05.071.
[45] D. Li, R. Li, M. Lu, X. Lin, Y. Zhan, L. Jiang, Carbon dioxide reforming of methane over Ru catalysts supported on Mg-Al oxides: a highly dispersed and stable Ru/Mg (Al) O catalyst, Appl. Catal. B Environ. 200 (2017) 566–577, https://doi.org/10.1016/j.apcatb.2016.07.050.
[46] J. Feng, L. Liu, X. Ju, M. Wang, X. Zhang, J. Wang, P. Chen, Sub-nanometer Ru clusters on ceria nanorods as efficient catalysts for ammonia synthesis under mild conditions, ACS Sustain. Chem. Eng. 10 (2022) 10181–10191, https://doi.org/10.1021/acssuschemeng.2c01635.
[47] B. Lin, B. Fang, Y. Wu, C. Li, J. Ni, X. Wang, J. Lin, C.-t. Au, L. Jiang, Enhanced ammonia synthesis activity of ceria-supported ruthenium catalysts induced by CO activation, ACS Catal. 11 (2021) 1331–1339, https://doi.org/10.1039/C9CC07385J.
[48] T. Yan, W. Bing, M. Xu, Y. Li, Y. Yang, G. Cui, L. Yang, M. Wei, Acid–base sites synergistic catalysis over Mg–Zr–Al mixed metal oxide toward synthesis of diethyl carbonate, RSC Adv. 8 (2018) 4695–4702, https://doi.org/10.1039/C7RA13629C.
[49] R. Dębek, M. Radlik, M. Motak, M.E. Galvez, W. Turek, P. Da Costa, T. Grzybek, Ni-containing Ce-promoted hydrotalcite derived materials as catalysts for methane reforming with carbon dioxide at low temperature–on the effect of basicity, Catal. Today 257 (2015) 59–65, https://doi.org/10.1016/j.cattod.2015.03.017.
[50] M.A. Naeem, D.B. Burueva, P.M. Abdala, N.S. Bushkov, D. Stoian, A. V. Bukhtiyarov, I.P. Prosvirin, V.I. Bukhtiyarov, K.V. Kovtunov, I.V. Koptyug, Deciphering the nature of Ru sites in reductively exsolved oxides with electronic and geometric metal–support interactions, J. Phys. Chem. C 124 (2020) 25299–25307, https://doi.org/10.1021/acs.jpcc.0c07203.
[51] B. Fang, F. Liu, C. Zhang, C. Li, J. Ni, X. Wang, J. Lin, B. Lin, L. Jiang, Sacrificial sucrose strategy achieved enhancement of ammonia synthesis activity over a ceria-supported Ru catalyst, ACS Sustain. Chem. Eng. 9 (2021) 8962–8969, https://doi.org/10.1021/acssuschemeng.1c01275.
[52] J. Li, Z. Liu, D.A. Cullen, W. Hu, J. Huang, L. Yao, Z. Peng, P. Liao, R. Wang, Distribution and valence state of Ru species on CeO_2 supports: support shape effect and its influence on CO oxidation, ACS Catal. 9 (2019) 11088–11103, https://doi.org/10.1021/acscatal.9b03113.
[53] L. Huang, X.-F. Liu, J. Zou, X. Duan, Z.-C. Chen, Z.-H. Zhou, L. Ye, X. Liang, S.-Y. Xie, Y. Yuan, Atomic ruthenium stabilized on vacancy-rich boron nitride for selective hydrogenation of esters, J. Catal. 406 (2022) 115–125, https://doi.org/10.1016/j.jcat.2022.01.004.
[54] M. Gao, J. Zhang, P. Zhu, X. Liu, Z. Zheng, Unveiling the origin of alkali metal promotion in CO_2 methanation over Ru/ZrO_2, Appl. Catal. B Environ. 314 (2022), 121476, https://doi.org/10.1016/j.apcatb.2022.121476.
[55] C.-F. Cao, K. Wu, C. Zhou, Y.-H. Yao, Y. Luo, C.-Q. Chen, L. Lin, L. Jiang, Electronic metal-support interaction enhanced ammonia decomposition efficiency of perovskite oxide supported ruthenium, Chem. Eng. Sci. 257 (2022), 117719, https://doi.org/10.1016/j.ces.2022.117719.
[56] N. Liu, M. Xu, Y. Yang, S. Zhang, J. Zhang, W. Wang, L. Zheng, S. Hong, M. Wei, $Au^{\delta-}$–Ov–Ti^{3+} interfacial site: catalytic active center toward low-temperature water gas shift reaction, ACS Catal. 9 (2019) 2707–2717, https://doi.org/10.1021/acscatal.8b04913.
[57] O.D. Pavel, D. Tichit, I.-C. Marcu, Acido-basic and catalytic properties of transition-metal containing Mg–Al hydrotalcites and their corresponding mixed oxides, Appl. Clay Sci. 61 (2012) 52–58, https://doi.org/10.1016/j.clay.2012.03.006.
[58] X. Fang, Y. Liu, W. Cen, Y. Cheng, Birnessite as a highly efficient catalyst for low-temperature NH_3-SCR: the vital role of surface oxygen vacancies, Ind. Eng. Chem. Res. 59 (2020) 14606–14615, https://doi.org/10.1021/acs.iecr.0c00188.
[59] J.H. Shin, G.J. Kim, S.C. Hong, Reaction properties of ruthenium over Ru/TiO_2 for selective catalytic oxidation of ammonia to nitrogen, Appl. Surf. Sci. 506 (2020), 144906, https://doi.org/10.1016/j.apsusc.2019.144906.
[60] L. Zhang, H. He, Mechanism of selective catalytic oxidation of ammonia to nitrogen over Ag/Al2O3, J. Catal. 268 (2009) 18–25, https://doi.org/10.1016/j.jcat.2009.08.011.
[61] S.D. Lin, A.C. Gluhoi, B.E. Nieuwenhuys, Ammonia oxidation over Au/MOx/γ-Al_2O_3—activity, selectivity and FTIR measurements, Catal. Today 90 (2004) 3–14, https://doi.org/10.1016/j.cattod.2004.04.047.
[62] C. Li, S. Yu, Y. Shi, M. Li, B. Fang, J. Lin, J. Ni, X. Wang, B. Lin, L. Jiang, Combining silica to boost the ammonia synthesis activity of ceria-supported Ru catalyst, Chem. Eng. Sci. 262 (2022), 118045, https://doi.org/10.1016/j.ces.2022.118045.
[63] Y. Qiu, E. Fu, F. Gong, R. Xiao, Catalyst support effect on ammonia decomposition over Ni/$MgAl_2O_4$ towards hydrogen production, Int. J. Hydrog. Energy 47 (2022) 5044–5052, https://doi.org/10.1016/j.ijhydene.2021.11.117.
[64] L. Zhang, R. Li, L. Cui, Z. Sun, L. Guo, X. Zhang, Y. Wang, Y. Wang, Z. Yu, T. Lei, Boosting photocatalytic ammonia synthesis performance over OVs-Rich Ru/$W_{18}O_{49}$: Insights into the roles of oxygen vacancies in enhanced hydrogen spillover effect, Chem. Eng. J. 461 (2023), 141892, https://doi.org/10.1016/j.cej.2023.141892.
[65] C. Li, M. Li, Y. Zheng, B. Fang, J. Lin, J. Ni, B. Lin, L. Jiang, Revealing hydrogen migration effect on ammonia synthesis activity over ceria-supported Ru catalysts, Appl. Catal. B Environ. 320 (2023), 121982, https://doi.org/10.1016/j.apcatb.2022.121982.
[66] B. Cao, H. Shi, Q. Sun, Y. Yu, L. Chang, S. Xu, C. Zhou, H. Zhang, J. Zhao, Y. Zhu, Electron deficiency modulates hydrogen adsorption strength of Ru single-atomic catalyst for efficient hydrogen evolution, Renew. Energy (2023), https://doi.org/10.2139/ssrn.4354822.